Theoretical Approach to Evaluate the Gas-Sensing Performance of Graphene Nanoribbon/Oligothiophene Composites

Ayesha Ashraf, John M. Herbert, Shabbir Muhammad, Bilal Ahmad Farooqi, Umar Farooq, Muhammad Salman, and Khurshid Ayub*

ACCESS | 📊 Metrics & More | 📖 Article Recommendations | 🆘 Supporting Information

ABSTRACT: Composite formation with graphene is an effective approach to increase the sensitivity of polythiophene (nPT) gas sensors. The interaction mechanism between gaseous analytes and graphene/nPT composite systems is still not clear, and density functional theory calculations are used to explore the interaction mechanism between graphene/nPT nanoribbon composites (with n = 3−9 thiophene units) and gaseous analytes CO, NH_3, SO_2, and NO_2. For the studied analytes, the interaction energy ranges from −44.28 kcal/mol for ($C_{54}H_{30}$-3PT)-NO_2 to −2.37 kcal/mol for ($C_{54}H_{30}$-3PT)-CO at the counterpoise-corrected ωB97M-V/def2-TZVPD level of theory. The sensing mechanism is further evaluated by geometric analysis, ultraviolet−visible spectroscopy, density of-states analysis, calculation of global reactivity indices, and both frontier and natural bond orbital analyses. The variation in the highest occupied molecular orbital/lowest unoccupied molecular orbital gap of the composite indicates the change in conductivity upon complexation with the analyte. Energy decomposition analysis reveals that dispersion and charge transfer make the largest contributions to the interaction energy. The graphene/oligothiophene composite is more sensitive toward these analytes than either component taken alone due to larger changes in the orbital gap. The computational framework established in the present work can be used to evaluate and design graphene/nPT nanoribbon composite materials for gas sensors.
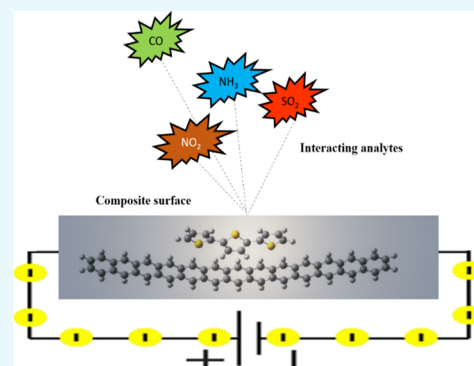
INTRODUCTION

Electronic devices which consist of sensing materials are generally regarded as chemical sensors. These chemical sensors interact with an analyte and transduce this interaction into an electrical or optical signal. The sensitivity, selectivity, and rapid detection of targeted molecules are the key factors in the design of advanced chemical sensors.[1] Conducting organic polymers, including polyaniline,[2,3] polypyrrole,[4,5,80] polyacetylene, and polythiophene,[6,7] are considered promising materials in the fabrication of smart materials due to their favorable electronic, optical, and magnetic properties and ease of functionalization. Among these materials, polythiophene is considered especially auspicious due to its low cost, better electrical conductivity, high environmental stability, and easy processing for applications in photovoltaics, electronics, electrocatalysis, sensors, and actuators.[8] Conducting polymers interact with various gases through electrochemical or acid−base interactions.[9−11] A polythiophene matrix is introduced with various nanofillers such as metals or metal oxides to enhance the electrical conductivity and thermomechanical properties.[12,13]

The development of polymer composites based on carbon fillers such as carbon nanotubes (CNTs) and graphene (GR) has gained much attention.[14] These polymer composites

provide a path to obtaining new sensor materials with better mechanical stability and functional properties than pure components. The high electrical conductivity and large surface area are remarkable features of these carbon allotropes, which are useful for the design of a chemical sensor that responds to electrical or chemical perturbations.[15] Two-dimensional graphene has potential as a gas-sensing material owing to the high surface area to volume ratio.[16] The electronic properties of graphene are altered on gas adsorption, which enables graphene to detect gases such as NH_3,[17−19] SO_2,[20] H_2,[9] and NO_2[21] with high precision. Graphene-based gas sensors have been extensively used due to their high carrier mobility, mechanical strength, and astounding optical and electronic properties. Graphene with one atom-thick layer has a significant role in sensing several gases such as NH_3, NO_2, H_2O, and CO with a detection limit of 1 ppb.[22] Hybrid materials of graphene can be used to design and regulate the
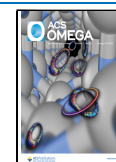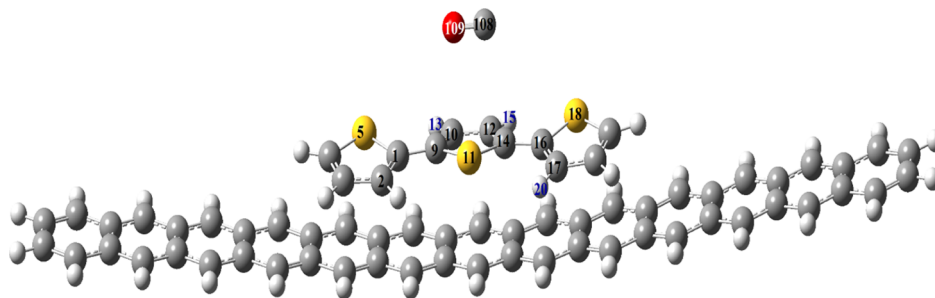
Figure 1. Reference geometry for the numbering scheme: $C_{54}H_{30}\cdots 3PT\cdots X$ (X = CO, NH$_3$, SO$_2$, NO$_2$).

sensing performance. The processes included may be the catalytic reaction with analyte, charge transfer, charge carrier transport, and manipulation of heterojunctions and their combinations.[23]

The theoretical studies indicate that the adsorption of different gases on graphene introduces inconsistent doping states.[24,25] The blending of pure graphene with other functional materials increases the sensitivity of graphene toward gas molecules due to the symbiotic effects of various components. Carbon−polymer composite-based chemiresistors possess great stability, improved lifetime, tunable selectivity, reversibility, and reproducibility.[26] Semiconductors,[27] carbon materials,[28] and organic/inorganic composites[29,30] are all used as sensing materials, but they function based on different mechanisms and principles. The conductive carbon particles in these systems allow the passage of current through continuous pathways between the parallel electrodes of the transducer. The polymer film swells up upon sorption of chemical vapor and some of the continuous pathways are interrupted, which increases the resistance of the composite. Therefore, solvation parameters are considered key to designing polymer-based sensors that are selective to various classes of volatile organic components.[31]

In situ chemical polymerization[32] and plasma methods[14] are used to synthesize graphene/polythiophene composites. The functionalized polythiophene/graphene nanostructures are synthesized to study the variation in their optoelectronic properties.[33] Poly(methyl methacrylate) chemically blended with graphene enhances carrier scattering properties and serves as an adsorbent layer to concentrate gas molecules on the surface of graphene.[34] The synthesis of polythiophene/ graphene oxide (PT/GrO) composites by interfacial polymerization is achieved to evaluate their electrical and electrochemical properties.[8] The graphene/polythiophene composites with different mass proportions are synthesized for their use as supercapacitor electrodes.[35] The theoretical insights of graphene/polythiophene composites with various sheet and ribbon models of graphene and different proportions of oligothiophene (*n*PT) in these composites are obtained to study the variation in the optical band gap.[36] The molecular-level dispersion of graphene is related to the efficiency of GR-conducting polymer composites that protects the intrinsic electronic properties of graphene and permits the homogeneous distribution of nanofillers by an appropriate selection of the polymer matrix through π−π stacking or van der Waals interactions.[1] Stacking interactions play an important role in controlling the structure and molecular recognition. Therefore, dispersion forces are important for their interaction with aromatic, polycyclic, and planar ligands. The interaction of molecules with other molecules or particle changes the

electronic structure as well as the charge distribution.[37] The other type of interactions is CH⋯π and lone-pair⋯π interactions that play a significant role in structural manifestation. The lone-pair⋯π interactions are mostly repulsive, that is, between non-bonding electrons and π electrons. The binding energies for these interactions lie in the range of ∼1−2 kcal/mol.[38] The oxidative or reductive gas molecules adsorbed on the surface of the graphene−polymer composite persuades the doping or de-doping of the polymer component, which results in the change in conductance of the composite.

All these eye-catching properties of polymeric-GR based materials make them perfect candidates for replacing the ordinary heavy sensing equipment with high-tech highly sensitive next-generation gas sensor materials.[39,40] Polythiophene thin films, derivatives, microstructures, and nanofibers have been explored experimentally as sensors for gases and oxidizing vapors including H$_2$S, NH$_3$,[6,41] CH$_3$OH, C$_2$H$_5$OH,[6,42] NO$_2$, Cl$_2$, SO$_2$,[43,44] and volatile organic compounds.[45] The hybridization of polythiophene with graphene provides many advantages in the gas-sensing performance. There are few reports about the use of hybrids of graphene, polythiophene, or its derivatives for gas detection. The hybrid of reduced graphene oxide and poly(3,4-ethylenedioxythiophene) is used for the sensing of NO$_2$ at room temperature.[46,47] Self-assembled functionalized polythiophene and graphene are used for the sensing of toxic ions, nitroaromatics, and surfactants.[33]

Herein, we examine a graphene−polythiophene nanoribbon model (C$_{54}$H$_{30}$-*n*PT) as a potential sensing material for gaseous analytes such as CO, NH$_3$, SO$_2$, and NO$_2$. The presence of these gases in ambient environments is hazardous, even at ppm and ppb concentrations. Therefore, their detection is important but as of yet there is no theoretical insight in the literature regarding the adsorption of gases on graphene−polythiophene composite surfaces. The present study aims to explain the sensing mechanism of gases over composite surfaces by examining the geometrical structures of C$_{54}$H$_{30}$-*n*PT before and after interaction with the aforementioned gas molecules. Estimation of interaction energies, frontier molecular orbital analysis, energy decomposition analysis, natural bond orbital (NBO) analysis of charge transfer, noncovalent interaction (NCI) analysis, and UV−vis spectroscopic analysis are performed to check the selectivity and sensitivity of sensors.

■ RESULTS AND DISCUSSION

Geometrical Parameters. Geometry optimization is important to ascertain the most stable structure. The geometries of different graphene sheets (C$_{30}$H$_{14}$, C$_{46}$H$_{18}$, and

$C_{59}H_{20}$) and ribbons ($C_{38}H_{22}$, $C_{46}H_{26}$, and $C_{54}H_{30}$), in composites with nPTs (n = 1−13) are examined in vertical, tilted, and π-stacking orientations. Stable composites are obtained in the π-stacked configuration as the size of the graphene model increases, see Figure 1 for an example. The ribbon models of graphene/nPT composites gave large interaction energies and stable complexes.[36] As such, we selected a $C_{54}H_{30}$-nPT graphene ribbon/nPT model for sensing gaseous analytes. Geometries of graphene−polythiophene nanoribbon composites, $C_{54}H_{30}$-nPT (n = 3, 5, 7, 9), were optimized both in isolation, and in complexes with CO, NH_3, SO_2, and NO_2 analytes. In the composite complexes, the analyte-to-composite distance, interlayer distance (between the nPT and the graphene ribbon), bond angle, and dihedral angle are important parameters that characterize the interaction between the composite and analyte. The analyte-to-composite distance characterizes the interaction of the graphene-nPT composite with the analyte, while the bond and dihedral angles indicate whether the composite is planar upon complexation.

The length of the nPT varies in these composites while the size of graphene ribbon remains the same. Analytes are oriented on the surface of the composite from the nPT side, in order to study the change in the geometry and interaction behavior. The geometries of nanoribbon composites ($C_{54}H_{30}$-nPT) with analytes (CO, NH_3, SO_2 and NO_2) are optimized. The optimized geometrical parameters are given in Table 1. The numbering scheme for the $C_{54}H_{30}$-3PT-X is shown in Figure 1 for X = CO.

$C_{54}H_{30}$-nPT-CO. Geometry of isolated composites changes after interactions with carbon monoxide. Different orientations of CO molecules are considered on the composite surface in recognition of the fact that CO may adopt either a carbene-like (:C=Ö) or a dipolar ($^-$C≡O$^+$) resonance structure. The

stable geometry is found to consist of a parallel orientation of CO on the composite surface, where both oxygen and carbon interact with nPT. The optimized geometry of $C_{54}H_{30}$-3PT-CO is depicted in Figure 2 and other less stable geometries are given in Figures S2 and S3.

The intermolecular bond distance $d_{S11-C108}$ in $C_{54}H_{30}$-3PT-CO is 3.57 Å and $d_{S11-O109}$ is 3.48 Å, whereas the interlayer distance between nPT and graphene ribbon is 3.63 Å. The interlayer distance in the larger nPT composite $C_{54}H_{30}$-5PT-CO increases to 3.96 Å as the graphene ribbon bends at the center. The bond distance $d_{S11-C108}$ decreases to 3.47 Å and $d_{S11-O109}$ increases to 3.58 Å. This decrease in the $d_{S11-C108}$ bond distance indicates a favorable interaction between S and C than S and O as the $d_{S11-O109}$ bond distance increases. In the $C_{54}H_{30}$-7PT-CO complex, the $d_{S11-C108}$ bond distance increases to 3.55 Å, whereas the interlayer and $d_{S11-O109}$ distances decrease to 3.86 and 3.52 Å, respectively. This decrease in the interlayer distance results as nPT (7PT) becomes parallel to the graphene ribbon, but the increase in the $d_{S11-C108}$ distance indicates a decrease in the interaction between CO and higher nPT composites. The interlayer distance in $C_{54}H_{30}$-9PT-CO is slightly smaller still, at 3.83 Å, due to the bending of the nPT with the graphene ribbon at the center. The $d_{S11-C108}$ intermolecular distance slightly decreases to 3.54 Å, whereas the $d_{S11-O109}$ bond distance remains the same at 3.52 Å. These changes indicate the variation in the interaction strength among graphene-nPT composites and CO. The variations in the interlayer distance between the $C_{54}H_{30}$ ribbon and nPT indicate the strength of π-stacking interactions.

The impact of the intermolecular angle $\angle C_{14}S_{11}X$ (X = C_{108}, O_{109}) on the overall complex formation has also been examined. The $\angle C_{14}S_{11}C_{108}$ and $\angle C_{14}S_{11}O_{109}$ bond angles in $C_{54}H_{30}$-3PT-CO are 63 and 78°, respectively. These $\angle C_{14}S_{11}C_{108}$ and $\angle C_{14}S_{11}O_{109}$ angles increase to 71 and 87° in $C_{54}H_{30}$-5PT-CO, respectively. The bond angle increases to minimize repulsion between bonding electrons. In $C_{54}H_{30}$-7PT-CO, the $\angle C_{14}S_{11}C_{108}$ and $\angle C_{14}S_{11}O_{109}$ angles decrease to 64 and 78°, respectively. The nPT becomes parallel over the graphene ribbon in all other complexes, so a decrease in bond angles is observed as the bond distance also increases in this complex. The $\angle C_{14}S_{11}C_{108}$ and $\angle C_{14}S_{11}O_{109}$ angles in the $C_{54}H_{30}$-9PT-CO complex are 66 and 80°, respectively. This increase in the angle is again due to changes in the geometry of the composite as both nPT and graphene ribbon bend at the center, and this change is in accordance with the bond distance. Another geometrical parameter is the dihedral angle that is influential in the planarity of the composites after complexation (i.e., conductivity change). The dihedral angle between two planes is the measure of coplanarity, and the $\angle S_{11}C_9C_1S_5$ dihedral angle varies after interaction with the analyte. It is 163° in the $C_{54}H_{30}$-3PT composite and increases to 165° after complexation with CO. The increase in the dihedral angle signifies a decrease in coplanarity. In $C_{54}H_{30}$-5PT, the dihedral angle is 165° and decreases to 163° in $C_{54}H_{30}$-5PT-CO. Similarly, the dihedral angle in $C_{54}H_{30}$-7PT is 169° and slightly decreases to 168° in $C_{54}H_{30}$-7PT-CO. The dihedral angle of $C_{54}H_{30}$-9PT composite decreases from 172 to 170° after complexation with CO in the $C_{54}H_{30}$-9PT-CO complex. This decrease in the dihedral angle increases the coplanarity. The overall variation in geometrical parameters is due to changes in the geometry of composites when nPT becomes bent and parallel over the graphene ribbon.

Table 1. Optimized Geometric Parameters of $C_{54}H_{30}$··· nPT···X Composite−Analyte Complexes, for n = 3, 5, 7, and 9 Thiophene Units and for Analytes X = CO, NH_3, SO_2, and NO_2[a]

system	$d(S_{11}\text{-}X_{108})$ Å[a]	$\angle C_{14}S_{11}X$[a] (degrees)	$\angle S_{11}C_9C_1S_5$ (degrees)
$C_{54}H_{30}$···3PT			163
$C_{54}H_{30}$···3PT···CO	3.57	63	165
$C_{54}H_{30}$···3PT···NH$_3$	3.60	71	165
$C_{54}H_{30}$···3PT···SO$_2$	3.55	84	166
$C_{54}H_{30}$···3PT···NO$_2$	3.53	68	170
$C_{54}H_{30}$···5PT			165
$C_{54}H_{30}$···5PT···CO	3.47	71	163
$C_{54}H_{30}$···5PT···NH$_3$	3.63	80	163
$C_{54}H_{30}$···5PT···SO$_2$	3.55	83	166
$C_{54}H_{30}$···5PT···NO$_2$	3.53	69	170
$C_{54}H_{30}$···7PT			169
$C_{54}H_{30}$···7PT···CO	3.55	64	168
$C_{54}H_{30}$···7PT···NH$_3$	3.62	70	168
$C_{54}H_{30}$···7PT···SO$_2$	3.56	88	170
$C_{54}H_{30}$···7PT···NO$_2$	3.42	62	173
$C_{54}H_{30}$···9PT			172
$C_{54}H_{30}$···9PT···CO	3.54	66	170
$C_{54}H_{30}$···9PT···NH$_3$	3.62	71	171
$C_{54}H_{30}$···9PT···SO$_2$	3.56	89	170
$C_{54}H_{30}$···9PT···NO$_2$	3.52	69	173

[a]Computed at the M06-2X/6-31G** level of theory.
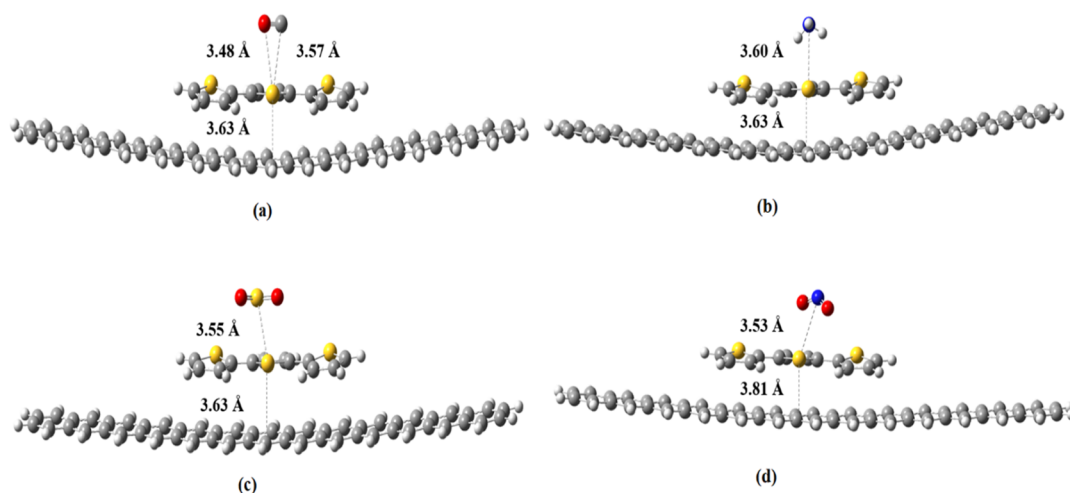
Figure 2. Optimized geometries of (a) $C_{54}H_{30}\cdots 3PT\cdots CO$, (b) $C_{54}H_{30}\cdots 3PT\cdots NH_3$, (c) $C_{54}H_{30}\cdots 3PT\cdots SO_2$, and (d) $C_{54}H_{30}\cdots 3PT\cdots NO_2$ composite−analyte complexes.

$C_{54}H_{30}$-nPT-NH$_3$. The optimized geometrical parameters of $C_{54}H_{30}$-nPT composite change upon complexation with NH$_3$ (Table 1). The optimized geometry of $C_{54}H_{30}$-3PT-NH$_3$ is given in Figure 2 and other less stable structures are given in Figures S2 and S3. The analyte-to-composite distance ($d_{S11-N108}$) in the $C_{54}H_{30}$-3PT−NH$_3$ complex is 3.60 Å and the interlayer distance is 3.63 Å. The $d_{S11-N108}$ intermolecular distance increases to 3.64 Å in $C_{54}H_{30}$-5PT-NH$_3$ and the interlayer distance increases to 3.96 Å due to the bending of the graphene ribbon at the center. The increase in the intermolecular distance indicates a decrease in interaction strength between NH$_3$ and the composite. The $d_{S11-N108}$ distance in the larger $C_{54}H_{30}$-7PT-NH$_3$ complex slightly decreases to 3.62 Å and remains the same in the $C_{54}H_{30}$-9PT-NH$_3$ complex. The interlayer distance decreases to 3.86 Å in $C_{54}H_{30}$-7PT-NH$_3$ as nPT becomes parallel to the graphene surface. This distance further decreases to 3.83 Å in the $C_{54}H_{30}$-9PT-NH$_3$ complex due to the bending of nPT and graphene ribbon at the center. The $\angle C_{14}S_{11}N_{108}$ bond angle in the $C_{54}H_{30}$-3PT-NH$_3$ complex is 71° and increases to 80° in the $C_{54}H_{30}$-5PT-NH$_3$ complex. The graphene ribbon is bent at the center and the central thiophene ring of the 5PT becomes slightly flat over the graphene ribbon and the interacting angle varies. In the $C_{54}H_{30}$-7PT−NH$_3$ complex, the angle decreases to 70° and then slightly increases to 71° in the $C_{54}H_{30}$-9PT−NH$_3$ complex. This variation is due to changes in the geometry of the composite, which is parallel in $C_{54}H_{30}$-7PT-NH$_3$ and then bent slightly at the center in the $C_{54}H_{30}$-9PT-NH$_3$ complex. The bond angle varies as the bond distance changes. The $\angle S_{11}C_9C_1S_5$ dihedral angle of the $C_{54}H_{30}$-3PT composite is 163° and increases to 165° after complexation with NH$_3$ in $C_{54}H_{30}$-3PT-NH$_3$. The increase in the dihedral angle decreases the coplanarity. In $C_{54}H_{30}$-5PT, the dihedral angle is 165° and decreases to 163° in $C_{54}H_{30}$-5PT- NH$_3$. The dihedral angle in $C_{54}H_{30}$-7PT is 169° and slightly decreases to 168° after complexation with NH$_3$ in $C_{54}H_{30}$-7PT- NH$_3$. The decrease in the dihedral angle ($\angle S_{11}C_9C_1S_5$) increase the coplanarity. The dihedral angle of the $C_{54}H_{30}$-9PT composite is 172° and in the $C_{54}H_{30}$-9PT-NH$_3$ complex, it decreases to 171°.

$C_{54}H_{30}$-nPT-SO$_2$. The optimized geometry of $C_{54}H_{30}$-3PT-SO$_2$ is depicted in Figure 2, whereas other less stable geometries are shown in Figures S2 and S3. The impact of geometrical parameters for these composite−analyte systems is

also elucidated and listed in Table 1. The analyte-to-composite distance ($d_{S11-S108}$) in the $C_{54}H_{30}$-3PT-SO$_2$ complex is 3.55 Å and remains the same in the $C_{54}H_{30}$-5PT-SO$_2$ complex. The interlayer distances in $C_{54}H_{30}$-3PT-SO$_2$ and $C_{54}H_{30}$-5PT-SO$_2$ complexes are 3.63 Å and 3.96 Å, respectively. The intermolecular distance ($d_{S11-S108}$) slightly increases to 3.56 Å in $C_{54}H_{30}$-7PT-SO$_2$ and does not change in the $C_{54}H_{30}$-9PT-SO$_2$ complex. SO$_2$ is oriented on the composite surface in a bent or V shape and its distance does not change much as the size of nPT increases in the composite. The interlayer distance decreases to 3.86 Å in $C_{54}H_{30}$-7PT-SO$_2$ and 3.83 Å in $C_{54}H_{30}$-9PT-SO$_2$ complexes in which 7PT is parallel over the graphene ribbon and 9PT becomes slightly bent at the center, respectively. The change in intermolecular angle $\angle C_{14}S_{11}S_{108}$ in all $C_{54}H_{30}$-nPT-SO$_2$ complexes is comparatively greater than all other composite/analyte complexes. The SO$_2$ is V-shaped and the sulfur atom of SO$_2$ is slightly displaced away from the interacting sulfur of the nPT. The intermolecular angle ($\angle C_{14}S_{11}S_{108}$) in the $C_{54}H_{30}$-3PT-SO$_2$ complex is 84°, and it slightly decreases to 83° in the $C_{54}H_{30}$-5PT-SO$_2$ complex. This is a negligible variation in the intermolecular angle as the bond distances in $C_{54}H_{30}$-3PT-SO$_2$ and $C_{54}H_{30}$-5PT-SO$_2$ remain the same. Then, a slight increase of 88° is observed in $C_{54}H_{30}$-7PT-SO$_2$, which further increases to 89° in the $C_{54}H_{30}$-9PT-SO$_2$ complex. This increase is due to a change in the position of nPT in these composites. This change in intermolecular angle results in a decrease in the interaction between SO$_2$ and higher graphene-nPT composites. The variation in the dihedral angle ($\angle S_{11}C_9C_1S_5$) also shows the same trend as the intermolecular angle. The $\angle S_{11}C_9C_1S_5$ dihedral angle of the $C_{54}H_{30}$-3PT composite is 163°, and it increases to 166° after interaction with SO$_2$ in $C_{54}H_{30}$-3PT-SO$_2$. In $C_{54}H_{30}$-5PT, the dihedral angle is 165° and increases to 166° in $C_{54}H_{30}$-5PT-SO$_2$. This increase in the dihedral angle decreases the coplanarity. The $C_{54}H_{30}$-5PT-SO$_2$ complex shows an increase in the dihedral angle than $C_{54}H_{30}$-5PT-CO and $C_{54}H_{30}$-5PT-NH$_3$, which is due to the V-shape geometry of SO$_2$ and the strength of interaction. The dihedral angle in $C_{54}H_{30}$-7PT is 169° and slightly increases to 170° in $C_{54}H_{30}$-7PT-SO$_2$. This slight increase is due to the planarity of nPT (7PT) over the graphene ribbon. $\angle S_{11}C_9 C_1 S_5$ increases the coplanarity. The dihedral angle ($\angle S_{11}C_9 C_1 S_5$) of the $C_{54}H_{30}$-9PT composite is

172° and in the $C_{54}H_{30}$-9PT-SO_2 complex, it decreases to 170° and coplanarity increases slightly which increases conjugation.

$C_{54}H_{30}$-nPT-NO_2. The optimized geometry of $C_{54}H_{30}$-3PT-NO_2 is shown in Figure 2 and other less stable geometries are given in Figures S2 and S3. The results of computed geometrical parameters of these composite–analyte systems are listed in Table 1. The analyte-to-composite distance ($d_{S11-N110}$) in the $C_{54}H_{30}$-3PT-NO_2 complex is 3.53 Å and remains invariable in the $C_{54}H_{30}$-5PT-NO_2 complex. The nPT become planar over the graphene ribbon (Figures 1 and S2). The interlayer distance in $C_{54}H_{30}$-3PT-NO_2 is 3.81 Å, and it slightly increases to 3.82 Å in $C_{54}H_{30}$-5PT-NO_2, which is due to the sliding of nPT over the graphene ribbon. The intermolecular distance ($d_{S11-N110}$) decreases to 3.42 Å in $C_{54}H_{30}$-7PT-NO_2 as NO_2 becomes parallel and slightly moves ahead to interfacing sulfur of nPT than the orientation of NO_2 in other composites (Figure S3). The nPT also becomes parallel to the graphene ribbon in this composite system and the interlayer distance decreases to 3.73 Å. The ($d_{S11-N110}$) intermolecular distance then increases to 3.52 Å, which indicates the decrease in interactions between NO_2 and $C_{54}H_{30}$-9PT composite. The interlayer distance is 3.73 Å. The intermolecular angle ($\angle C_{14}S_{11}N_{110}$) in $C_{54}H_{30}$-3PT-NO_2 is 68° and slightly increases to 69° in the $C_{54}H_{30}$-5PT-NO_2 complex. The intermolecular angle decreases to 62° in $C_{54}H_{30}$-7PT-NO_2 and then increases to 69° in the $C_{54}H_{30}$-9PT-NO_2 complex. This change in the intermolecular angle causes either an increase or decrease in the interaction between the NO_2 and the composites. The $\angle S_{11}C_9C_1S_5$ dihedral angle of the $C_{54}H_{30}$-3PT composite is 163° and it increases to 170° after complexation with NO_2 in $C_{54}H_{30}$-3PT-NO_2. In $C_{54}H_{30}$-5PT, the dihedral angle is 165° and increases to 170° in $C_{54}H_{30}$-5PT-NO_2. The dihedral angle in $C_{54}H_{30}$-7PT is 169° and further increases to 173° after complexation with NO_2 in $C_{54}H_{30}$-7PT-NO_2. In $C_{54}H_{30}$-nPT-NO_2 complexes, the continuous increase is observed in the dihedral angle than all other complexes, which decreases the coplanarity. The anomalous behavior of NO_2 with the composite is due to its difference in polarity relative to the other analytes. The dihedral angle of the $C_{54}H_{30}$-9PT composite is 172° and in the $C_{54}H_{30}$-9PT-NO_2 complex, it increases to 173°.

Based on geometric parameters (intermolecular distances and angles) of all these complexes, it is clear that NO_2 shows the maximum change, indicating that it has the strongest interaction with the composites among the analytes considered here.

Interaction Energies. The strength of the interaction between the composites $C_{54}H_{30}$-nPT (n = 3, 5, 7, and 9) and selected analytes (CO, NH_3, SO_2, and NO_2) is studied at the ωB97M-V/def2-TZVPD level of theory. Interaction energies are provided in Table 2. The interaction energies of noncovalent complexes are generally overestimated because of the basis set superposition error (BSSE), which can be mitigated by counterpoise (CP) correction,[48] and results both with and without the CP correction are reported in Table 2.

At the ωB97M-V/def2-TZVPD level of theory, the CP corrections are quite modest, no more than 1.3 kcal/mol but usually much less, and in the discussion that follows we will quote the CP-corrected results. In contrast, interaction energies computed at the M06-2X-D3/6-31G(d,p) level of theory (not shown) exhibit considerable variation when the CP correction is applied and are therefore not considered further in the present work.

Table 2. Interaction Energies of $C_{54}H_{30}\cdots n$PT$\cdots$X Composite–Analyte Complexes (for X = CO, NH_3, SO_2, and NO_2)[a]

system	E_{int} (kcal/mol)	
	no CP	with CP
$C_{54}H_{30}\cdots$3PT$\cdots$CO	−2.8	−2.4
$C_{54}H_{30}\cdots$3PT$\cdots NH_3$	−3.3	−2.6
$C_{54}H_{30}\cdots$3PT$\cdots SO_2$	−16.7	−15.7
$C_{54}H_{30}\cdots$3PT$\cdots NO_2$	−45.0	−44.3
$C_{54}H_{30}\cdots$5PT$\cdots$CO	−2.3	−2.2
$C_{54}H_{30}\cdots$5PT$\cdots NH_3$	−3.0	−2.4
$C_{54}H_{30}\cdots$5PT$\cdots SO_2$	−5.5	−4.4
$C_{54}H_{30}\cdots$5PT$\cdots NO_2$	−33.1	−32.8
$C_{54}H_{30}\cdots$7PT$\cdots$CO	−2.3	−1.8
$C_{54}H_{30}\cdots$7PT$\cdots NH_3$	−2.9	−2.1
$C_{54}H_{30}\cdots$7PT$\cdots SO_2$	−5.1	−3.8
$C_{54}H_{30}\cdots$7PT$\cdots NO_2$	−14.8	−14.1
$C_{54}H_{30}\cdots$9PT$\cdots$CO	−2.2	−1.8
$C_{54}H_{30}\cdots$9PT$\cdots NH_3$	−2.7	−2.2
$C_{54}H_{30}\cdots$9PT$\cdots SO_2$	−2.1	−1.1
$C_{54}H_{30}\cdots$9PT$\cdots NO_2$	−3.9	−3.4

[a]Computed at the ωB97M-V/def2-TZVPD level of theory.

$C_{54}H_{30}$-nPT-CO. The interaction energy of $C_{54}H_{30}$-3PT-CO at the ωB97M-V/def2-TZVPD level is −2.8 kcal/mol (or −2.4 kcal/mol upon CP correction) and decreases to −2.3 kcal/mol (−2.2 kcal/mol with CP correction) in the $C_{54}H_{30}$-5PT-CO complex. The NCIs between a π system and a polar molecule leads to polar-π interactions,[49,50] and the strength of these interactions decreases upon increasing the length of the nPT constituent as the delocalization of π the electrons reduces the charge density available to CO for polar-π interaction. CO is a polar molecule and oriented over the composite so as to interact with the π electrons of the composite. The interaction energy of the $C_{54}H_{30}$-7PT-CO complex is −2.3 kcal/mol (−1.8 kcal/mol with CP) and it decreases to −2.2 kcal/mol (−1.8 kcal/mol with CP) in $C_{54}H_{30}$-9PT-CO. The interaction energies decrease as conjugation in the π system and the length of nPT chain increase, for the reasons described above.

$C_{54}H_{30}$-nPT-NH_3. Ammonia is a trigonal pyramidal asymmetric polar molecule. The noncovalent polar-π interaction energies of the $C_{54}H_{30}$-nPT-NH_3 complexes are listed in Table 2. The interaction energy of the $C_{54}H_{30}$-3PT-NH_3 complex is −3.3 kcal/mol (−2.6 kcal/mol with CP). This energy is greater than the $C_{54}H_{30}$-3PT-CO complex (−2.8 kcal/mol) because NH_3 is more polar than CO. The interaction energies decrease to −3.0 kcal/mol (−2.4 kcal/mol with CP) and −2.9 kcal/mol (−2.1 kcal/mol with CP) in the $C_{54}H_{30}$-5PT-NH_3 and $C_{54}H_{30}$-7PT-NH_3 complexes, respectively. The interaction energy further decreases to −2.7 kcal/mol (−2.2 kcal/mol with CP) in the $C_{54}H_{30}$-9PT-NH_3 complex. The strength of the polar-π NCI decreases with increasing delocalization of the π electrons because less charge is available to NH_3 in complexes with larger oligomers.

$C_{54}H_{30}$-nPT-SO_2. SO_2 exhibits a larger interaction energy with $C_{54}H_{30}$-nPT composites as compared to CO or NH_3. SO_2 is a bent V-shaped molecule and therefore polar, with oxygen withdrawing electron density from sulfur and polarizing the S–O bond. Polar-π interactions are generated between the electropositive sulfur and the conjugated π system. The interaction energies of $C_{54}H_{30}$-nPT-SO_2 complexes are given in Table 2. The interaction energy of $C_{54}H_{30}$-3PT-SO_2 is

−16.7 kcal/mol (−15.7 kcal/mol with CP). The interaction energy decreases to −5.5 kcal/mol (−4.4 kcal/mol with CP) and −5.1 kcal/mol (−3.8 kcal/mol with CP) in the $C_{54}H_{30}$-5PT-SO_2 and $C_{54}H_{30}$-7PT-SO_2 complexes, respectively. This sharp decrease in the interaction energy from −16.7 kcal/mol ($C_{54}H_{30}$-3PT-SO_2) to −5.1 kcal/mol ($C_{54}H_{30}$-7PT-SO_2) is due to the decreasing strength of polar-π interactions and an increase in $\pi-\pi$ interactions with an increase in size of nPT. As compared to larger composites, in $C_{54}H_{30}$-3PT-SO_2 there is not much delocalization of π electrons within the conjugated system because of the smaller size of nPT. As a result, the π electrons are easily available to the electropositive sulfur in $C_{54}H_{30}$-3PT-SO_2 and the interaction energy is much larger. In $C_{54}H_{30}$-9PT-SO_2, the interaction energy further decreases to −2.1 kcal/mol (−1.1 kcal/mol with CP).

$C_{54}H_{30}$-nPT-NO_2. The interaction energy of $C_{54}H_{30}$-3PT-NO_2 is −45.0 kcal/mol (−44.3 kcal/mol with CP). This value is much greater that the corresponding values for another analytes (CO, NH_3, or SO_2). In NO_2, nitrogen is surrounded by two electronegative oxygens and it is also smaller in size than oxygen. The withdrawing effect of electronegative oxygen creates more positive charge density on the nitrogen atom leading to favorable interactions with the π electrons, resulting in a strong polar-π interaction. The interaction energy decreases to −33.1 kcal/mol (−32.8 kcal/mol with CP) in the $C_{54}H_{30}$-5PT−NO_2 complex and further decreases to −14.8 kcal/mol (−14.1 kcal/mol with CP) and −3.9 kcal/mol (−3.4 kcal/mol with CP) in $C_{54}H_{30}$-7PT-NO_2 and $C_{54}H_{30}$-9PT-NO_2, respectively. As with other systems considered above, increasing delocalization of the π electrons with increasing polymer length reduces the strength of the analyte−composite polar-π interaction. In combination with the survey of the optimized geometrical parameters, these interaction energies make clear that NO_2 exhibits the strongest interaction with the composite.

Natural Bond Orbital Analysis. Charge transfer may play a significant role in electronic properties and changes in molecular charge upon complexation may help to account for the sensing ability of the composite substrate toward analytes. Here, the amount of charge transfer between the graphene-nPT composite and the analyte is investigated using the natural atomic charges that come from NBO analysis, as listed in Table 3.

Overall, we find that complexation transfer a small negative charge to the analyte. The amount of charge transferred is quite small (no more than 0.005e) when the analyte is CO or NH_3 and does not change appreciably with the size of the nPT oligomer, in contrast to the interaction energies that do depend on size. The transferred charge is larger in the case of SO_2, which develops a charge of −0.039e upon complexation. This increase, relative to CO or NH_3, can be ascribed to resonance structures in SO_2 that allow it to accommodate more charge. Finally, the amount of charge transferred to the analyte is most significant in the case of NO_2, where it exceeds −0.3e. This is consistent with the much stronger interactions of NO_2 with the composites, as compared to other analytes.

Frontier Molecular Orbital Analysis. We next analyze the interaction of the composites with the analytes in terms of their effect on the HOMO−LUMO (H−L) gap. These frontier orbital energies are listed in Table 4, whereas the orbitals themselves are plotted in Figures 3 and S4−S6. The change in HOMO and LUMO energies due to the overlapping of frontier molecular orbitals upon complexation dictates

Table 3. Natural Population Analysis of Composite−Analyte Complexes $C_{54}H_{30}$···nPT···X (n = 3, 5, 7, and 9; X = CO, NH_3, SO_2, and NO_2)

system	amount of charge transfer		
	nPT	graphene	analyte
$C_{54}H_{30}$···3PT	+0.027	−0.027	
$C_{54}H_{30}$···3PT···CO	+0.030	−0.025	−0.005
$C_{54}H_{30}$···3PT···NH_3	+0.023	−0.022	−0.001
$C_{54}H_{30}$···3PT ···SO_2	+0.057	−0.018	−0.039
$C_{54}H_{30}$···3PT···NO_2	+0.066	+0.244	−0.310
$C_{54}H_{30}$···5PT	+0.058	−0.058	
$C_{54}H_{30}$···5PT···CO	+0.060	−0.058	−0.002
$C_{54}H_{30}$···5PT···NH_3	+0.056	−0.055	−0.001
$C_{54}H_{30}$···5PT···SO_2	+0.092	−0.054	−0.038
$C_{54}H_{30}$···5PT···NO_2	+0.083	+0.249	−0.333
$C_{54}H_{30}$···7PT	+0.071	−0.071	
$C_{54}H_{30}$···7PT···CO	+0.075	−0.070	−0.005
$C_{54}H_{30}$···7PT···NH_3	+0.069	−0.068	−0.001
$C_{54}H_{30}$···7PT···SO_2	+0.086	−0.047	−0.038
$C_{54}H_{30}$···7PT···NO_2	+0.085	+0.241	−0.326
$C_{54}H_{30}$···9PT	+0.064	−0.064	
$C_{54}H_{30}$···9PT···CO	+0.068	−0.063	−0.005
$C_{54}H_{30}$···9PT···NH_3	+0.316	−0.315	−0.001
$C_{54}H_{30}$···9PT···SO_2	+0.110	−0.070	−0.039
$C_{54}H_{30}$···9PT···NO_2	+0.087	+0.326	−0.324

changes in conductivity of the system.[51−53] Changes in the H−L gap of the composite upon complexation with an analyte can be expected due to changes induced in the torsional angles of the composite, leading to increased twisting of the conjugated system and therefore a larger H−L gap in the presence of an analyte.[54,55] The increase in the H−L gap of the composite after sensing increases its resistance which lowers its conductivity.

$C_{54}H_{30}$-nPT-CO. The H−L gaps in $C_{54}H_{30}$-nPT are 0.63, 0.59, 0.58, and 0.58 eV for n = 3, 5, 7, and 9, respectively. Upon complexation with CO, these gaps increase slightly, for example, to 0.65 eV for n = 3, although the effect saturates for larger oligomers and for n = 9, the H−L gap of the $C_{54}H_{30}$-9PT-CO complex is 0.58 eV. These modifications of the gap are expected to manifest as a decrease in conductivity in the presence of the analyte.

$C_{54}H_{30}$-nPT-NH_3. The H−L gap of $C_{54}H_{30}$-nPT also increases upon complexation with NH_3, for example, to 0.65 eV in the n = 3 oligomer, although the effect once again saturates quickly as a function of the oligomer size.

$C_{54}H_{30}$-nPT-SO_2. In contrast to the case of CO or NH_3, the H−L gap of the composite decreases very slightly in the presence of the analyte to 0.63 eV for n = 3, although for larger oligomers there is essentially no change in the gap upon complexation with the analyte.

$C_{54}H_{30}$-nPT-NO_2. The $C_{54}H_{30}$-nPT composites show a considerable variation in the H−L gap after interaction with NO_2. In $C_{54}H_{30}$-3PT, the H−L gap is 0.63 eV and it increases to 0.86 eV upon complexation with NO_2, whereas the gap in $C_{54}H_{30}$-5PT increases from 0.59 to 0.65 eV in the presence of NO_2. The H−L gap in this system exhibits a significant variation with respect to the size of the composite, as it is larger once again (at 0.84 eV) for n = 7 and then smaller (0.62 eV) for n = 9.

Electronic Properties and Global Indices. The quantities $-E_{HOMO}$ and $-E_{LUMO}$ are approximations to the ionization

Table 4. H−L Gaps, λ_{max}, Oscillator Strengths, and Excitation Energies of $C_{54}H_{30}\cdots nPT\cdots X$ Composite−Analyte Complexes (n = 3, 5, 7, and 9; X = CO, NH$_3$, SO$_2$, and NO$_2$)[a]

system	H−L gap (eV)	λ_{max} (nm)	oscillator strength	excitation energy (eV)	HOMO (eV)	LUMO (eV)
$C_{54}H_{30}\cdots 3PT$	0.63	590	3.61	2.10	−3.85	−3.22
$C_{54}H_{30}\cdots 3PT\cdots CO$	0.65	603	5.23	2.06	−3.88	−3.23
$C_{54}H_{30}\cdots 3PT\cdots NH_3$	0.65	595	2.88	2.08	−3.92	−3.27
$C_{54}H_{30}\cdots 3PT\cdots SO_2$	0.63	604	5.11	2.05	−3.92	−3.29
$C_{54}H_{30}\cdots 3PT\cdots NO_2$	0.86	808	2.47	1.53	−4.07	−3.21
$C_{54}H_{30}\cdots 5PT$	0.59	652	1.81	1.90	−3.78	−3.19
$C_{54}H_{30}\cdots 5PT\cdots CO$	0.60	656	1.81	1.89	−3.79	−3.19
$C_{54}H_{30}\cdots 5PT\cdots NH_3$	0.58	651	2.11	1.90	−3.82	−3.24
$C_{54}H_{30}\cdots 5PT\cdots SO_2$	0.59	651	1.93	1.90	−3.82	−3.23
$C_{54}H_{30}\cdots 5PT\cdots NO_2$	0.65	845	1.51	1.47	−4.02	−3.37
$C_{54}H_{30}\cdots 7PT$	0.58	664	1.39	1.87	−3.77	−3.19
$C_{54}H_{30}\cdots 7PT\cdots CO$	0.59	663	1.50	1.87	−3.78	−3.19
$C_{54}H_{30}\cdots 7PT\cdots NH_3$	0.58	662	2.12	1.87	−3.81	−3.23
$C_{54}H_{30}\cdots 7PT\cdots SO_2$	0.58	665	2.02	1.86	−3.82	−3.24
$C_{54}H_{30}\cdots 7PT\cdots NO_2$	0.84	822	1.80	1.51	−4.03	−3.19
$C_{54}H_{30}\cdots 9PT$	0.58	680	2.06	1.82	−3.76	−3.18
$C_{54}H_{30}\cdots 9PT\cdots CO$	0.58	680	2.05	1.82	−3.77	−3.19
$C_{54}H_{30}\cdots 9PT\cdots NH_3$	0.58	680	1.96	1.82	−3.80	−3.22
$C_{54}H_{30}\cdots 9PT\cdots SO_2$	0.59	683	1.89	1.82	−3.80	−3.21
$C_{54}H_{30}\cdots 9PT\cdots NO_2$	0.62	820	2.42	1.51	−4.01	−3.39

[a]Computed at the (TD-)B3LYP/6-31G** level of theory.
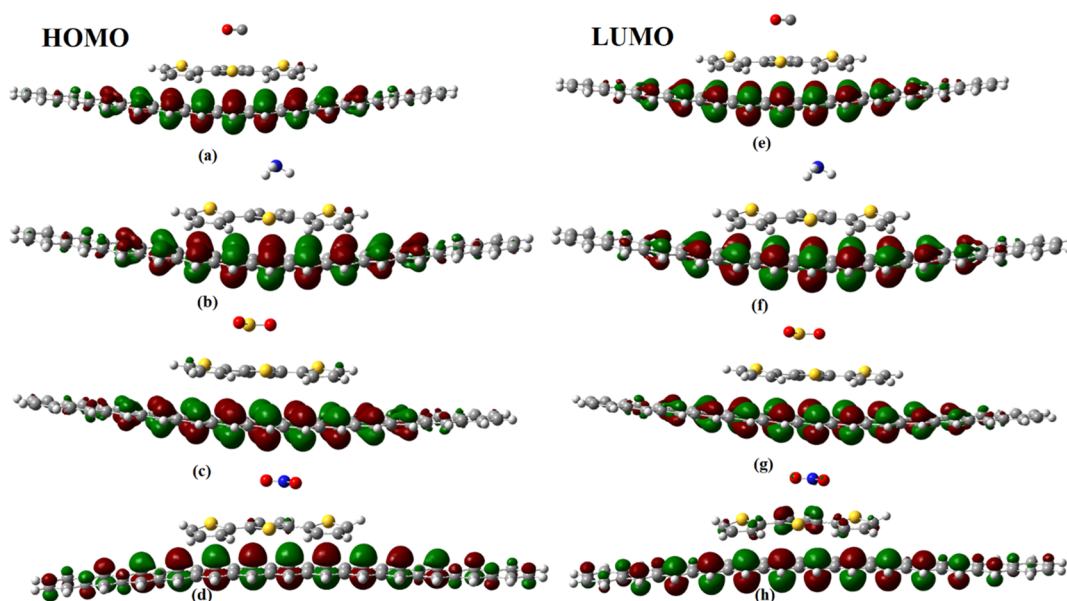
Figure 3. HOMOs and LUMOs of (a,e) $C_{54}H_{30}\cdots 3PT\cdots CO$, (b,f) $C_{54}H_{30}\cdots 3PT\cdots NH_3$, (c,g) $C_{54}H_{30}\cdots 3PT\cdots SO_2$, and (d,h) $C_{54}H_{30}\cdots 3PT\cdots NO_2$ composite−analyte complexes.

potential (IP) and the electron affinity (EA), respectively. IP, EA, and global indices, including chemical potential (μ), chemical hardness (η), softness (s) electrophilicity (ω),[84] values are given in Table S1. The ionization potential decreases as the size of nPT increases in the composite. The IP in $C_{54}H_{30}$-3PT is 3.86 eV. The IP decreases to 3.78 eV in $C_{54}H_{30}$-5PT, 3.77 eV in $C_{54}H_{30}$-7PT, and 3.76 eV in $C_{54}H_{30}$-9PT composites. The IPs increase in the presence of the analytes, with the largest changes occurring in the case of NO$_2$ and, for example, the IP of $C_{54}H_{30}$-3PT-NO$_2$ is 4.45 eV. The HOMO energies of $C_{54}H_{30}$-3PT changes by 0.02, 0.05, 0.06, and 0.60 eV in the presence of CO, NH$_3$, SO$_2$, and NO$_2$, respectively, which is the same order as in the case of the charge-transfer

analysis. Similarly, the $C_{54}H_{30}$-nPT-NO$_2$ complexes have lower EAs than other complexes.

The global reactivity indices are very important to determine the reactivity and stability of complexes. The global hardness is the resistance of a species to deformation under the influence of an electric field. The reactivity of species decreases but the stability of a system increases with increase in hardness.[56] The chemical hardness of the $C_{54}H_{30}$-3PT composite increases after complexation with CO, NH$_3$, SO$_2$, and NO$_2$ but decreases as the size of nPT increases. The increase in chemical hardness results in decrease in reactivity but increase in stability. Softness is the reciprocal of chemical hardness, and its increases with the length of nPT. The values of the chemical

potential also increase after sensing the analytes, which indicates the reactivity of the composite sensor toward analytes. The electrophilicity (ω) also provides data about the stability and reactivity of complexes. The results in the variation of global indices are in accordance with the results of other properties (*vide supra*).

UV–Vis Absorption Studies. The electronic excitation properties in terms of charge transfer and optical band gaps play a significant role in comprehending the conductivity and sensitivity of the interacting species.[57] Time-dependent density functional theory (TD-DFT) results at the B3LYP/6-31G** level, including λ_{max}, excitation energies and oscillator strength of $C_{54}H_{30}$-nPT (n = 3, 5, 7, 9) and their complexes ($C_{54}H_{30}$-nPT-X), are listed in Table 4. The simulated UV–vis spectra of $C_{54}H_{30}$-3PT-X are shown in Figure 4, whereas the spectra of
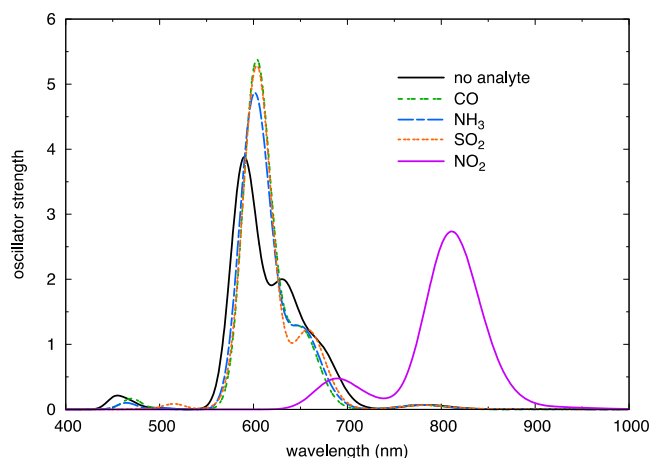
Figure 4. UV–vis spectra of $C_{54}H_{30}\cdots$3PT, $C_{54}H_{30}\cdots$3PT$\cdots$CO, $C_{54}H_{30}\cdots$3PT$\cdots$NH$_3$, $C_{54}H_{30}\cdots$3PT$\cdots$SO$_2$, and $C_{54}H_{30}\cdots$3PT$\cdots$NO$_2$ composite–analyte complexes, computed at the TD-B3LYP/6-31G** level.

other complexes are given in Figure 2 and S7–S9. These spectra were computed from the lowest 40 singlet excitation energies, using Gaussian broadening with a width parameter of 0.05 eV.

$C_{54}H_{30}$-nPT-CO. The observed λ_{max} of the $C_{54}H_{30}$-3PT composite is 590 nm, and it is red shifted to 603 nm upon complexation with CO. The absorption maximum of the $C_{54}H_{30}$-5PT composite appears at 652 nm and increases to 656 nm in the $C_{54}H_{30}$-5PT-CO complex. The increase in absorption maxima from 603 to 656 nm is due to increased conjugation with increasing chain length of the oligomer, as well as a decrease in the band gap within the complexes. The λ_{max} of $C_{54}H_{30}$-7PT is 664 nm and remains essentially unchanged after complexation with CO. The non-bonding electrons on the oxygen atom may lead to π-antibonding interactions and therefore a larger shift in absorption spectra. The same is true for $C_{54}H_{30}$-9PT. Apparently, complexation with CO does not perturb the absorption spectrum of a sufficiently large composite.

$C_{54}H_{30}$-nPT-NH$_3$. The $C_{54}H_{30}$-nPT-NH$_3$ complexes show a minimal variation in their absorption maxima. The λ_{max} of the $C_{54}H_{30}$-3PT composite is 590 nm and shows red shift to 595 nm upon the interaction with NH$_3$, whereas λ_{max} shifts from 652 nm in $C_{54}H_{30}$-5PT to 651 nm in the $C_{54}H_{30}$-5PT-NH$_3$ complex. Absorption maxima in $C_{54}H_{30}$-7PT and $C_{54}H_{30}$-9PT (664 nm and 680 nm, respectively) shift by ≤2 nm upon

complexation with NH$_3$. As with the CO complexes, the $C_{54}H_{30}$-nPT-NH$_3$ complexes show a very small change in their absorption maxima and this is consistent with less charge transfer in these complexes.

$C_{54}H_{30}$-nPT-SO$_2$. The $C_{54}H_{30}$-nPT-SO$_2$ complexes also exhibit minimal changes in their absorption spectra upon complexation. Although λ_{max} of $C_{54}H_{30}$-3PT shifts from 590 to 604 nm upon complexation with SO$_2$, in the larger complexes the shift is ≤3 nm.

$C_{54}H_{30}$-nPT-NO$_2$. The red shift in the absorption maximum of $C_{54}H_{30}$-3PT is very pronounced upon complexation with NO$_2$, shifting from 590 nm to 808 nm, and for larger $C_{54}H_{30}$-nPT composites, the absorption maximum shifts from 652 nm to 845 nm (n = 5), from 664 nm to 822 nm (n = 7), and from 680 nm to 820 nm (n = 9). In the last two cases, the absorption maximum shifts into the near-IR region. These very pronounced shifts are due to increased conjugation within the composite and unpaired electrons of the nitrogen atom in NO$_2$.

Density-of-States Analysis. Density-of-states (DOS) analysis helps in exploring the interaction between the composites and the analytes during sensing, by approximating the number of energy states that might be available to an electron at specific energies. In a DOS spectrum (i.e., the spectrum of Kohn–Sham orbital eigenvalues), relatively small variations in the region of the HOMO and LUMO are expected to bring obvious changes in the corresponding electric conductivity.[56] The LUMO peaks of $C_{54}H_{30}$-nPT are observed at −3.22 eV (n = 3), −3.19 eV (n = 5 and n = 7), and −3.18 eV (n = 9). The HOMO peaks are located at −3.85, −3.78, −3.77 and −3.76 eV for n = 3, 5, 7, and 9, respectively. Figure 5 shows the DOS spectra of $C_{54}H_{30}$-3PT and $C_{54}H_{30}$-3PT-X, with the analogous spectra for larger oligomers shown in Figures S10–S12.

The HOMO energy of $C_{54}H_{30}$-nPT increases as the number of nPT units increases and, after interaction with analytes, new occupied energy states (HOMO) are generated which facilitate the transfer of electrons between the composite and analytes. Moreover, the interaction with analytes varies the peak maxima at different energy levels and this variation in the peak intensity is considered as an optimal condition for the working mechanism of chemical sensors. The new virtual orbitals in $C_{54}H_{30}$-3PT-X are seen at −3.23, −3.27, −3.29, and −2.56 eV for X = CO, NH$_3$, SO$_2$, and NO$_2$, respectively. The considerable variation in the optical band gap of $C_{54}H_{30}$-3PT-NO$_2$ is due to the formation of a new orbital at −2.56 eV. The change in the HOMO and LUMO energies with respect to the length of the nPT is small (Table 4). The pronounced variation in the position of HOMO and LUMO that is observed for X = SO$_2$ or NO$_2$, as compared to X = CO or NH$_3$, is consistent with the overall low sensitivity of these composites toward the latter two analytes. The variation in the shape and intensity of peaks demonstrates that the transport of electrons can either increase or decrease upon complexation.

NCI Analysis. NCI analysis is used for visualizing NCIs in real space, which is based on quantum mechanical electron density and its derivatives;[58,59] specifically, the reduced density gradient (RDG), which measures deviation from a homogeneous electron distribution:

$$s(\mathbf{r}) = \frac{1}{2(3\pi^2)} \frac{|\nabla\rho(\mathbf{r})|}{\rho(\mathbf{r})^{4/3}} \tag{1}$$
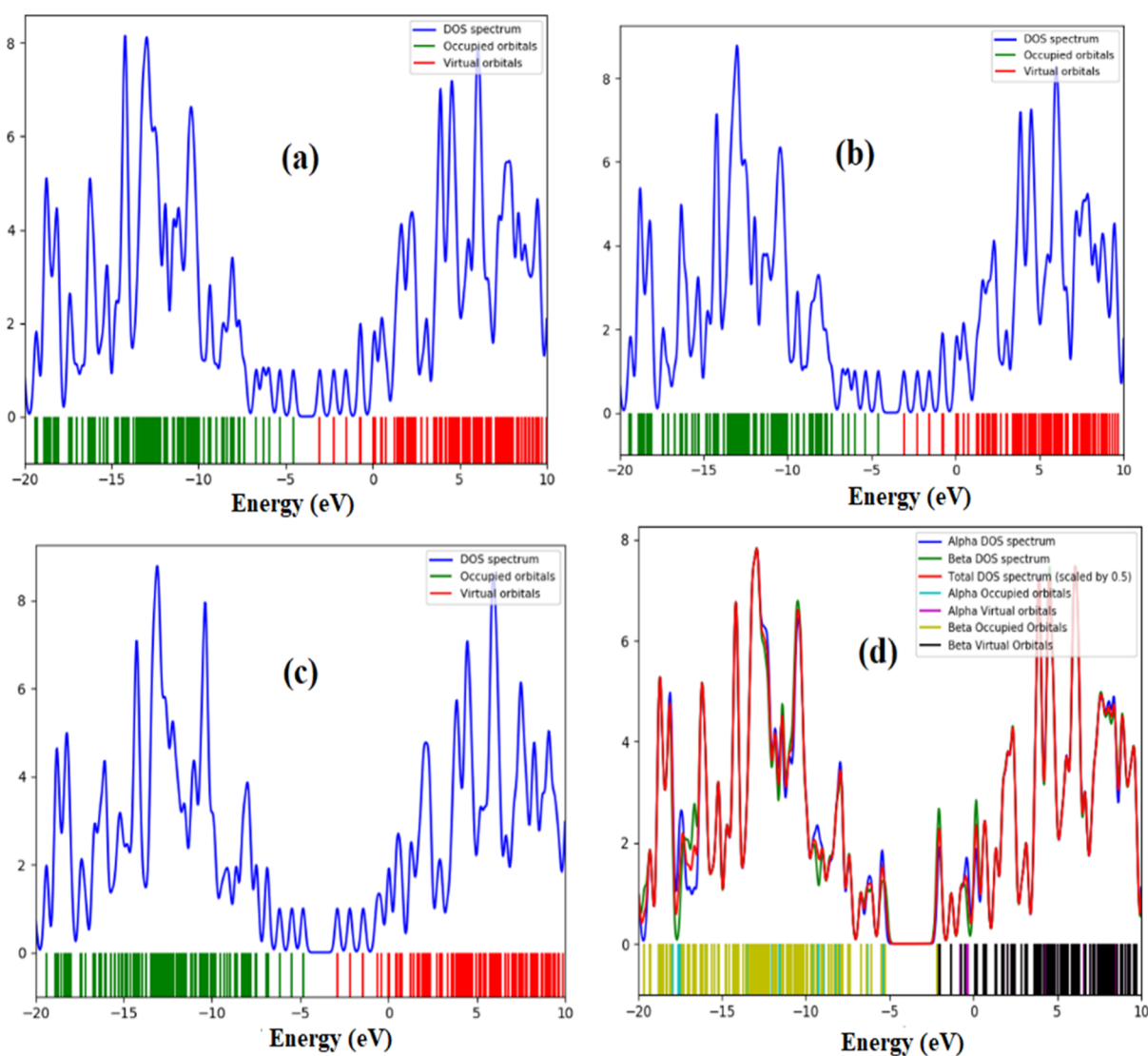
Figure 5. Spectra of Kohn−Sham eigenvalues of (a) $C_{54}H_{30}\cdots 3PT\cdots CO$, (b) $C_{54}H_{30}\cdots 3PT\cdots NH_3$, (c) $C_{54}H_{30}\cdots 3PT \cdots SO_2$, and (d) $C_{54}H_{30}\cdots 3PT\cdots NO_2$.

NCI analysis distinguishes color-coded RDG isosurfaces as dispersion interactions, hydrogen bonds, or repulsive steric interactions. The RDG regions are colored as blue (strong) or green (weak) for attractive interactions and red (strong) or yellow (weak) for repulsive interactions. The blue region also represents the hydrogen bonding and green region represents the dispersion interactions. The three eigenvalues ($\lambda_1 \leq \lambda_2 \leq \lambda_3$) of the Laplacian of the density are computed in order to determine the different types of non-bonded interactions. All of these eigenvalues are negative at nuclei where density approaches a local maximum.

For covalent interactions, two of the eigenvalues are negative but the third is positive. Finally, the second eigenvalue is positive for steric interactions and this value is employed to differentiate the regions of the covalent and non-covalent interactions. The covalent and non-covalent interaction regions have negative eigenvalue ($\lambda_2 < 0$), whereas for steric interactions $\lambda_2 > 0$. The stronger NCIs have higher density values while weaker interactions have lower density values as the strength of interactions is related to the magnitude of $s(\mathbf{r})$. Figure 6 shows color-mapped isosurfaces of $s(\mathbf{r})$, using an isocontour value of 0.5 a.u., and their respective scatter plots

versus sign (λ_2) $\rho(\mathbf{r})$, which defines the NCI plot, for $C_{54}H_{30}\cdots$ 3PT and $C_{54}H_{30}\cdots$3PT-X. Analogous plots for other complexes can be found in Figures S13−S15. The color-mapped $s(\mathbf{r})$ isosurface of $C_{54}H_{30}\cdots$3PT shows dispersion interactions across an isosurface that closely resembles the contours of the atomic van der Waals radii, which is typical of π-stacking interactions.[60,61] In the NCI scatter plot, dispersion interactions appear at low density [sgn(λ_2) $\rho < -0.01$ a.u.] and strongly repulsive interactions at larger densities [sgn(λ_2) $\rho \sim 0.02-0.04$ a.u.].

Energy Decomposition Analysis. While NCI plots can be used to obtain a qualitative view of NCIs, the (second-generation) absolutely localized molecular orbital energy decomposition analysis (ALMO-EDA)[62−64] approach is used to quantitatively decompose interaction energies into physically meaningful components, as provided in Table 5 for the $C_{54}H_{30}\cdots n$PT-X complexes. The total interaction energy of these complexes is decomposed into ΔE_{PREP}, ΔE_{FRZ}, ΔE_{POL}, ΔE_{DISP}, and ΔE_{CT} terms. The "preparation energy" $\Delta E_{PREP} = \Delta E_{HYBRID} + \Delta E_{GEOM}$ includes both the energy required to change the hybridization state of the fragments, which is not only relevant in the context of NCIs but also the energy
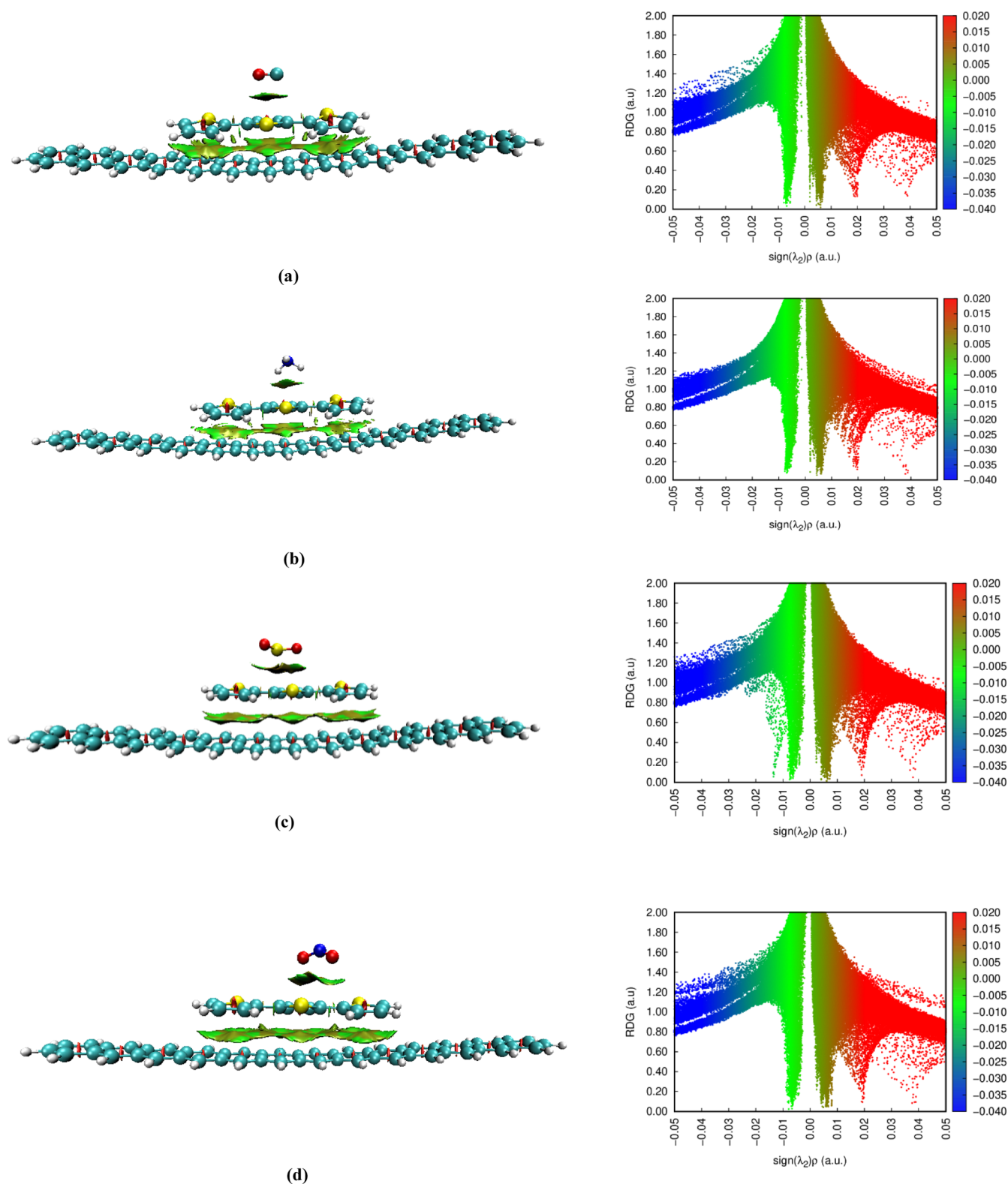
Figure 6. Color-mapped RDG isosurfaces (left) and NCI scatter diagrams (right) for $C_{54}H_{30}\cdots3PT\cdots X$ with (a) X = CO, (b) X = NH_3, (c) X = SO_2, and (d) X = NO_2.

ΔE_{GEOM} that is required to distort the geometry from its isolated-fragment value to the geometry in the supramolecular complex. The latter is significant only in the case of NO_2. The "frozen" energy component ΔE_{FRZ} includes both electrostatics (without polarization) and Pauli repulsion, that is , it is the energy associated with bringing the fragments together in the absence of density relaxation. In the present examples, this term is dominated by Pauli repulsion because the analytes are not large enough to experience significant electrostatic attraction. The dispersion term (ΔE_{DISP}) is a key component of the NCIs in these systems and is (unsurprisingly) relatively large, as supported by the NCI analysis. The polarization

Table 5. Second-Generation ALMO-EDA Results for $C_{54}H_{30}\cdots n$PT-X Complexes (X = CO, NH_3, SO_2, and NO_2), in kcal/mol

system	ΔE_{PREP}	ΔE_{FRZ}	ΔE_{POL}	ΔE_{DISP}	ΔE_{CT}	E_{int}
$C_{54}H_{30}\cdots$3PT$\cdots$CO	0.0	3.1	−0.1	−3.9	−2.0	−3.0
$C_{54}H_{30}\cdots$3PT$\cdots NH_3$	0.0	1.7	−0.2	−3.8	−2.2	−4.4
$C_{54}H_{30}\cdots$3PT$\cdots SO_2$	0.0	8.1	−0.9	−8.0	−6.1	−6.9
$C_{54}H_{30}\cdots$3PT$\cdots NO_2$	5.8	4.6	−36.0	−6.4	−2.7	−34.6
$C_{54}H_{30}\cdots$5PT$\cdots$CO	0.0	2.9	−0.1	−3.8	−1.8	−2.9
$C_{54}H_{30}\cdots$5PT$\cdots NH_3$	0.0	1.8	−0.2	−3.7	−2.2	−4.2
$C_{54}H_{30}\cdots$5PT$\cdots SO_2$	0.0	8.1	−0.9	−8.0	−6.0	−6.8
$C_{54}H_{30}\cdots$5PT$\cdots NO_2$	−15.1	4.6	−14.7	−6.3	−2.7	−34.2
$C_{54}H_{30}\cdots$7PT$\cdots$CO	0.0	2.9	−0.1	−3.8	−1.9	−2.8
$C_{54}H_{30}\cdots$7PT$\cdots NH_3$	0.0	1.9	−0.2	−3.5	−2.2	−4.1
$C_{54}H_{30}\cdots$7PT$\cdots SO_2$	0.0	8.0	−0.9	−7.8	−5.9	−6.6
$C_{54}H_{30}\cdots$7PT$\cdots NO_2$	−15.2	4.7	−14.8	−6.2	−2.7	−34.3
$C_{54}H_{30}\cdots$9PT$\cdots$CO	0.0	2.8	−0.1	−3.7	−1.9	−2.8
$C_{54}H_{30}\cdots$9PT$\cdots NH_3$	0.0	1.8	−0.2	−3.5	−2.2	−4.1
$C_{54}H_{30}\cdots$9PT$\cdots SO_2$	0.0	7.9	−0.9	−7.8	−5.9	−6.6
$C_{54}H_{30}\cdots$9PT$\cdots NO_2$	−15.3	4.7	−14.8	−6.3	−2.7	−34.4

energy (ΔE_{POL}) is rather small for each of the analytes except NO_2. Finally, the charge-transfer term ΔE_{CT} is not insignificant, demonstrating that a relatively small amount of the transferred change can manifest as several kcal/mol in the interaction energy. However, the largest values of ΔE_{CT} are observed in the case of SO_2 rather than NO_2; thus, the ALMO-EDA charge-transfer results do not correlate perfectly with the extent of charge transfer that is predicted by natural population analysis. (There is no particular reason that it should correlate perfectly, as the two procedures for defining charge transfer are different.) Except for the case of NO_2, where the polarization energy is quite large, the interactions in these complexes are dominated by the ΔE_{DISP} and ΔE_{CT} terms.

CONCLUSIONS

The detection of noxious gases in the environment is very important, and various sensor materials based upon conducting polymers and their composites are under investigation in this regard. Composites consisting of conducting polymers with graphene are of great interest to increase the sensitivity and performance of sensor devices, but the molecular mechanism is unclear. DFT calculations performed herein explore possible gas-sensing mechanisms in graphene/polythiophene composites, with the composite modeled as $C_{54}H_{30}\cdots n$PT for n = 3−9 thiophene units and exploring analytes CO, NH_3, SO_2, and NO_2. The trend of interaction energies between these analytes and the composite is $NO_2 > SO_2 > NH_3 > CO$. These differences arise due to variations in the strength of polar−π interactions. The interaction energies themselves range from an estimated value of −44.3 kcal/mol for $C_{54}H_{30}\cdots$3PT$\cdots NO_2$ to −2.4 kcal/mol for $C_{54}H_{30}\cdots$3PT$\cdots$CO.

Analysis of the frontier molecular orbitals may elucidate how the analyte induces conductivity changes in the composite sensor material. The H−L gap of the composite is found to increase upon complexation with each of the aforementioned analytes. UV−vis spectra of the composites red-shifts upon complexation of the analyte, and the predicted absorbance increases with increasing chain polymer length. The NBO analysis helps in identifying the charge donor and acceptor species during the sensing phenomenon and the amount of partial charges on individual atoms in composite/analyte complexes. NCI isosurfaces and scatter plots in terms of RDG reveal the nature of NCI regions in $C_{54}H_{30}\cdots n$PT$\cdots$X

complexes. The energy decomposition analysis (second-generation ALMO-EDA) provides a quantitative measurement of the NCIs and decompose them into different components that account for the contribution of each component toward the overall interaction energy. The dispersion and charge-transfer components contribute somewhat more than other components to the interaction energy term. Frontier molecular orbital analysis shows variation in the optical band gap of the composite and absorption maxima also red-shifted upon interaction with all analytes. One-electron DOS spectra indicate the observable change upon interaction with NO_2 and SO_2.

All these results point to the sensitivity of the $C_{54}H_{30}\cdots$3PT composite among other graphene-nPT chains (5PT, 7PT, 9PT), as several of the aforementioned changes upon complexation with the analyte are present in the 3PT composite but washed out as the length of the polymer increases. Furthermore, this study indicates that these composites are clearly more sensitive toward NO_2 as compared to other analytes, and to a lesser extent toward SO_2, with only small changes noted upon complexation with either CO or NH_3.

Computational Methodology. All calculations are performed using Q-Chem 5.2.[65] The Gauss View[66] and IQmol[67] graphical interfaces are used to visualize results. The graphene/nPT ribbon models exhibit larger interaction energies as compared to graphene/nPT sheet models.[68] Therefore, a $C_{54}H_{30}$-nPT graphene−polythiophene nanoribbon composite model is selected as a sensor material to check its sensitivity against various gaseous analytes: CO, NH_3, SO_2, and NO_2. Note that the H−L gap converges quickly with the molecular size in linear acenes,[69] justifying our use of the term "nanoribbons" for these materials.

Various possible orientations of each analyte on the composite surface are considered to obtain the lowest energy structure optimized at the M06-2X/6-31G(d,p)[70,71] level of theory. Frequency calculations are performed at the same level of theory to confirm these structures as true minima. Based on our previous work,[36] the M06-2X/6-31G(d,p), M06-2X-D3/6-31G(d,p),[72,73] M06-2X-D3/6-31G(d,p) (CP), and ωB97M-V/def2-TZVPD (CP) level of theories can be used for the reliable estimate of interaction energies, where "CP" indicates the counterpoise correction to reduce BSSE. We will use the

ωB97M-V/def2-TZVPD level of theory (with and without CP correction) to estimate interaction energies, as this is one of the best-performing DFT methods for energies,[74,75] although its use requires basis sets of triple-ζ quality.[76] For reasons of cost, structure optimizations are therefore performed at the M06-2X/6-31G(d,p) level. The SG-1 quadrature grid was used for B3LYP, the SG-2 grid for ωB97M-V, and the SG-3 grid for M06-2X.[77]

Interaction energies and their CP-corrected counterparts are calculated as

$$\Delta E_{\text{int}} = E_{\text{complex}} - [(E_{\text{composite}} + E_{\text{analyte}})] \quad (2)$$

$$\Delta E_{\text{int,CP}} = \Delta E_{\text{int}} - E_{\text{BSSE}} \quad (3)$$

where E_{complex} is the electronic energy of the composite–analyte complex, $E_{\text{composite}}$ is the electronic energy of the composite, and E_{analyte} is the electronic energy of the analyte. The quantity $E_{\text{int,CP}}$ is the CP-corrected interaction energy and E_{BSSE} is the CP correction defined as the monomer energies (composite and analyte) computed in the monomer basis set minus those computed in the supersystem basis set. B3LYP is a reliable method to calculate the electronic properties of materials based on conducting polymers.[3,78−81] Therefore, we have used B3LYP for the frontier molecular orbital (HOMO−LUMO) analysis and other electronic properties. Chemical potential (μ), hardness (η), softness (S), and electrophilicity (ω) are reactivity descriptors. The chemical potential is estimated (using Koopmans' theorem[82]) as

$$\mu = -(E_{\text{HOMO}} + E_{\text{LUMO}})/2 \quad (4)$$

where E_{HOMO} is the energy of the highest occupied molecular orbital and E_{LUMO} is the energy of lowest unoccupied molecular orbitals. A similar approach is used for the hardness

$$\eta = (E_{\text{LUMO}} - E_{\text{HOMO}})/2 \quad (5)$$

Softness and electrophilicity are computed using[83]

$$S = \frac{1}{2\eta} \quad (6)$$

$$\omega = \frac{\mu^2}{2\eta} \quad (7)$$

NBO analysis is used to study the distribution of atomic partial charges. The TD-DFT approach is used to simulate UV−vis spectra of the isolated and complexed structures, at the B3LYP/6-31G** level within the Tamm-Dancoff approximation. GaussSum software[84] is used to plot the DOS spectra. The Multiwfn 3.7 program[85] is used to make NCI plots,[58] which are color-mapped isosurfaces of the RDG, $s(\mathbf{r})$. The scatter plots are obtained by plotting RDG $s(\mathbf{r})$ versus sign(λ_2) ρ, where λ_2 is the second largest eigenvalue of the Hessian of electron density.[58] The VMD 1.9.3 program[86] is used to render isosurfaces of $s(\mathbf{r})$, with a contour value of 0.5 a.u. The second-generation ALMO-EDA[62−64,87] is used to further break down the interaction energy into physically meaningful components.

$$E_{\text{int}} = \Delta E_{\text{PREP}} + \Delta E_{\text{FRZ}} + \Delta E_{\text{POL}} + \Delta E_{\text{DISP}} + \Delta E_{\text{CT}} \quad (8)$$

ASSOCIATED CONTENT

SI **Supporting Information**

The Supporting Information is available free of charge at https://pubs.acs.org/doi/10.1021/acsomega.1c05863.

Optimized configurations of 5, 7, and 9 ribbon composites with analytes; calculation table for global reactivity indices; canonical depiction of complexes; UV−vis spectra; DOS plots; color-mapped isosurfaces; and scatter diagrams (PDF)

AUTHOR INFORMATION

Corresponding Author

Khurshid Ayub − *Department of Chemistry, COMSATS University Islamabad, Abbottabad 22060, Pakistan;* orcid.org/0000-0003-0990-1860; Phone: +92-992-383591-6; Email: khurshid@cuiatd.edu.pk; Fax: +92-992-383441

Authors

Ayesha Ashraf − *Department of Chemistry and Biochemistry, The Ohio State University, Columbus, Ohio 43210, USA;* Present Address: Present Address: Institute of Chemistry, University of the Punjab, Quaid-e-Azam Campus, Lahore 54590, Pakistan

John M. Herbert − *Department of Chemistry and Biochemistry, The Ohio State University, Columbus, Ohio 43210, USA;* orcid.org/0000-0002-1663-2278

Shabbir Muhammad − *Department of Physics, College of Science, King Khalid University, Abha 61413, Saudi Arabia;* orcid.org/0000-0003-4908-3313

Bilal Ahmad Farooqi − *Institute of Chemistry, University of the Punjab, Lahore 54590, Pakistan*

Umar Farooq − *Institute of Chemistry, University of the Punjab, Lahore 54590, Pakistan*

Muhammad Salman − *Institute of Chemistry, University of the Punjab, Lahore 54590, Pakistan*

Complete contact information is available at:
https://pubs.acs.org/10.1021/acsomega.1c05863

Author Contributions

A.A.: data curation, formal analysis, investigation, methodology, visualization, and writing—original draft; J.M.H.: investigation, methodology, visualization, software, validation, writing—review, and editing; M.S.: reviewing. B.A.F.: contribution in validation. U.F.: reviewing. M.S.: contribution in validation. K.A.: supervision, reviewing and editing

Notes

The authors declare no competing financial interest.

■ REFERENCES

(1) Avossa, J.; Paolesse, R.; Di Natale, C.; Zampetti, E.; Bertoni, G.; De Cesare, F.; Scarascia-Mugnozza, G.; Macagnano, A. Electrospinning of Polystyrene/Polyhydroxybutyrate Nanofibers Doped with Porphyrin and Graphene for Chemiresistor Gas Sensors. *Nanomaterials* 2019, 9, 280.

(2) Cogal, S.; Calio, L.; Celik Cogal, G.; Salado, M.; Kazim, S.; Oksuz, L.; Ahmad, S.; Uygun Oksuz, A. RF plasma-enhanced graphene-polymer composites as hole transport materials for perovskite solar cells. *Polym. Bull.* 2018, 75, 4531−4545.

(3) Ullah, H.; Shah, A.-u. -H. A.; Bilal, S.; Ayub, K. DFT Study of Polyaniline NH3, CO2, and CO Gas Sensors: Comparison with Recent Experimental Data. *J. Phys. Chem. C* 2013, 117, 23701−23711.

(4) Ullah, H.; Ayub, K.; Ullah, Z.; Hanif, M.; Nawaz, R.; Shah, A.-u. -H. A.; Bilal, S. Theoretical Insight of Polypyrrole Ammonia Gas Sensor. *Synth. Met.* 2013, 172, 14−20.

(5) Wasim, F.; Mahmood, T.; Ayub, K. An Accurate Cost Effective DFT Approach to Study Sensor Behaviour of Polypyrrole for Nitrate Ion in Gas and Aqueous Phase. *Phys. Chem. Chem. Phys.* 2016, 18, 19236−19247.

(6) Navale, S. T.; Mane, A. T.; Khuspe, G. D.; Chougule, M. A.; Patil, V. B. Room Temperature NO2 Sensing Properties of Polythiophene Films. *Synth. Met.* 2014, 195, 228−233.

(7) Ashraf, A.; Farooq, U.; Farooqi, B. A.; Ayub, K. Electronic Structure of Polythiophene Gas Sensors for Chlorinated Analytes. *J. Mol. Model.* 2020, 26, 44.

(8) Bora, C.; Pegu, R.; Saikia, B. J.; Dolui, S. K. Synthesis of Polythiophene/Graphene Oxide Composites by Interfacial Polymerization and Evaluation of Their Electrical and Electrochemical Properties. *Polym. Int.* 2014, 63, 2061−2067.

(9) Al-Mashat, L.; Shin, K.; Kalantar-Zadeh, K.; Plessis, J. D.; Han, S. H.; Kojima, R. W.; Kaner, R. B.; Li, D.; Gou, X.; Ippolito, S. J.; et al. Graphene/Polyaniline Nanocomposite for Hydrogen Sensing. *J. Phys. Chem. C* 2010, 114, 16168−16173.

(10) Bai, H.; Sheng, K.; Zhang, P.; Li, C.; Shi, G. Graphene Oxide/Conducting Polymer Composite Hydrogels. *J. Mater. Chem.* 2011, 21, 18653−18658.

(11) Bai, S.; Guo, J.; Sun, J.; Tang, P.; Chen, A.; Luo, R.; Li, D. Enhancement of NO2-Sensing Performance at Room Temperature by Graphene-Modified Polythiophene. *Ind. Eng. Chem. Res.* 2016, 55, 5788−5794.

(12) Lu, Q.; Zhou, Y. Synthesis of Mesoporous Polythiophene/MnO2 Nanocomposite and Its Enhanced Pseudocapacitive Properties. *J. Power Sources* 2011, 196, 4088−4094.

(13) Uygun, A.; Yavuz, A. G.; Sen, S.; Omastová, M. Polythiophene/SiO2 Nanocomposites Prepared in the Presence of Surfactants and Their Application to Glucose Biosensing. *Synth. Met.* 2009, 159, 2022−2028.

(14) Yu, X.; Cheng, H.; Zhang, M.; Zhao, Y.; Qu, L.; Shi, G. Graphene-Based Smart Materials. *Nat. Rev. Mater.* 2017, 2, 17046.

(15) Yuan, W.; Shi, G. Graphene-based gas sensors. *J. Mater. Chem. A* 2013, 1, 10078−10091.

(16) Wang, T.; Huang, D.; Yang, Z.; Xu, S.; He, G.; Li, X.; Hu, N.; Yin, G.; He, D.; Zhang, L. A Review on Graphene-Based Gas/Vapor Sensors with Unique Properties and Potential Applications. *Nano-Micro Lett.* 2016, 8, 95−119 SpringerOpen April 1.

(17) Singh, E.; Meyyappan, M.; Nalwa, H. S. Flexible Graphene-Based Wearable Gas and Chemical Sensors. *ACS Appl. Mater. Interfaces* 2017, 9, 34544−34586.

(18) Mackin, C.; Schroeder, V.; Zurutuza, A.; Su, C.; Kong, J.; Swager, T. M.; Palacios, T. Chemiresistive Graphene Sensors for Ammonia Detection. *ACS Appl. Mater. Interfaces* 2018, 10, 16169−16176.

(19) Schedin, F.; Geim, A. K.; Morozov, S. V.; Hill, E. W.; Blake, P.; Katsnelson, M. I.; Novoselov, K. S. Detection of Individual Gas Molecules Adsorbed on Graphene. *Nat. Mater.* 2007, 6, 652−655.

(20) Shokuhi Rad, A.; Esfahanian, M.; Maleki, S.; Gharati, G. Application of carbon nanostructures toward SO2 and SO3 adsorption: a comparison between pristine graphene and N-doped graphene by DFT calculations. *J. Sulfur Chem.* 2016, 37, 176−188.

(21) Pearce, R.; Iakimov, T.; Andersson, M.; Hultman, L.; Spetz, A. L.; Yakimova, R. Epitaxially grown graphene based gas sensors for ultra sensitive NO2 detection. *Sens. Actuators, B* 2011, 155, 451−455.

(22) Agrawal, A. V.; Kumar, N.; Kumar, M. Strategy and Future Prospects to Develop Room-Temperature-Recoverable NO2 Gas Sensor Based on Two-Dimensional Molybdenum Disulfide. *Nano-Micro Lett.* 2021, 13, 38.

(23) Jian, Y.; Hu, W.; Zhao, Z.; Cheng, P.; Haick, H.; Yao, M.; Wu, W. Gas Sensors Based on Chemi-Resistive Hybrid Functional Nanomaterials. *Nano-Micro Lett.* 2020, 12, 71.

(24) Huang, B.; Li, Z.; Liu, Z.; Zhou, G.; Hao, S.; Wu, J.; Gu, B.-L.; Duan, W. Adsorption of Gas Molecules on Graphene Nanoribbons and Its Implication for Nanoscale Molecule Sensor. *J. Phys. Chem. C* 2008, 112, 13442−13446.

(25) Leenaerts, O.; Partoens, B.; Peeters, F. M. Adsorption of H2O, NH3, CO, NO2, and NO on graphene: A first-principles study. *Phys. Rev. B: Condens. Matter Mater. Phys.* 2008, 77, 125416.

(26) Quercia, L.; Loffredo, F.; Di Francia, G. Influence of Filler Dispersion on Thin Film Composites Sensing Properties. *Sens. Actuators, B* 2005, 109, 153−158.

(27) Persaud, K. C. Polymers for Chemical Sensing. *Mater. Today* 2005, 8, 38−44.

(28) Miao, J.; Miyauchi, M.; Simmons, T. J.; Dordick, J. S.; Linhardt, R. J. Electrospinning of Nanomaterials and Applications in Electronic Components and Devices. *J. Nanosci. Nanotechnol.* 2010, 10, 5507−5519.

(29) Wang, C.; Yin, L.; Zhang, L.; Xiang, D.; Gao, R. Metal Oxide Gas Sensors: Sensitivity and Influencing Factors. *Sensors* 2010, 10, 2088−2106.

(30) Ding, B.; Wang, M.; Yu, J.; Sun, G. Gas Sensors Based on Electrospun Nanofibers. *Sensors* 2009, 9, 1609−1624.

(31) Grate, J. W.; Abraham, M. H.; Wise, B. M. Design and Information Content of Arrays of Sorption-Based Vapor Sensors Using Solubility Interactions and Linear Solvation Energy Relationships. In *Computational Methods for Sensor Material Selection*; Springer US, 2009, pp 193−218.

(32) Zhao, J.; Xie, Y.; Le, Z.; Yu, J.; Gao, Y.; Zhong, R.; Qin, Y.; Huang, Y. Preparation and Characterization of an Electromagnetic Material: The Graphene Nanosheet/Polythiophene Composite. *Synth. Met.* 2013, 181, 110−116.

(33) Maity, N.; Ghosh, R.; Nandi, A. K. Optoelectronic Properties of Self-Assembled Nanostructures of Polymer Functionalized Polythiophene and Graphene. *Langmuir* 2018, 34, 7585−7597.

(34) Dan, Y.; Lu, Y.; Kybert, N. J.; Luo, Z.; Johnson, A. T. C. Intrinsic Response of Graphene Vapor Sensors. *Nano Lett.* 2009, 9, 1472−1475.

(35) P. Melo, J.; Schulz, E. N.; Morales-Verdejo, C.; Horswell, S. L.; Camarada, M. B. Synthesis and Characterization of Graphene/Polythiophene (GR/PT) Nanocomposites: Evaluation as High-Performance Supercapacitor Electrodes. *Int. J. Electrochem. Sci.* 2017, 12, 2933−2948.

(36) Ashraf, A.; Carter-Fenk, K.; Herbert, J. M.; Farooqi, B. A.; Farooq, U.; Ayub, K.; Ayub, K. Interaction of Graphene Quantum Dots with Oligothiophene: A Comprehensive Theoretical Study. *J. Phys. Chem. C* 2019, 123, 29556−29570.

(37) Jissy, A. K.; Datta, A. Effect of External Electric Field on H-Bonding and π-Stacking Interactions in Guanine Aggregates. *ChemPhysChem* 2012, 13, 4163−4172.

(38) Nijamudheen, A.; Jose, D.; Shine, A.; Datta, A. Molecular Balances Based on Aliphatic CH−π and Lone-Pair−π Interactions. *J. Phys. Chem. Lett.* 2012, 3, 1493−1496.

(39) Liu, C.; Hsu, P.-C.; Lee, H.-W.; Ye, M.; Zheng, G.; Liu, N.; Li, W.; Cui, Y. Transparent air filter for high-efficiency PM2.5 capture. *Nat. Commun.* 2015, 6, 6205.

(40) Ramesan, M. T.; Santhi, V.; Bahuleyan, B. K.; Al-Maghrabi, M. A. Structural Characterization, Material Properties and Sensor Application Study of in Situ Polymerized Polypyrrole/Silver Doped

Titanium Dioxide Nanocomposites. *Mater. Chem. Phys.* **2018**, *211*, 343−354.

(41) Malkeshi, H.; Milani Moghaddam, H. Ammonia Gas-Sensing Based on Polythiophene Film Prepared through Electrophoretic Deposition Method. *J. Polym. Res.* **2016**, *23*, 108.

(42) Gonçalves, V. C.; Balogh, D. T. Optical Chemical Sensors Using Polythiophene Derivatives as Active Layer for Detection of Volatile Organic Compounds. *Sens. Actuators, B* **2012**, *162*, 307−312.

(43) Dua, V.; Surwade, S. P.; Ammu, S.; Zhang, X.; Jain, S.; Manohar, S. K. Chemical Vapor Detection Using Parent Polythiophene Nanofibers. *Macromolecules* **2009**, *42*, 5414−5415.

(44) Kumar, C.; Rawat, G.; Kumar, H.; Kumar, Y.; Ratan, S.; Prakash, R.; Jit, S. Poly (3, 3′″-dialkylquaterthiophene) Based Flexible Nitrogen Dioxide Gas Sensor. *IEEE Sensors Lett.* **2018**, *2*, 1−4.

(45) Li, B.; Santhanam, S.; Schultz, L.; Jeffries-EL, M.; Iovu, M. C.; Sauvé, G.; Cooper, J.; Zhang, R.; Revelli, J. C.; Kusne, A. G.; et al. Inkjet Printed Chemical Sensor Array Based on Polythiophene Conductive Polymers. *Sens. Actuators, B* **2007**, *123*, 651−660.

(46) Yang, Y.; Li, S.; Yang, W.; Yuan, W.; Xu, J.; Jiang, Y. In Situ Polymerization Deposition of Porous Conducting Polymer on Reduced Graphene Oxide for Gas Sensor. *ACS Appl. Mater. Interfaces* **2014**, *6*, 13807−13814.

(47) Dunst, K. J.; Scheibe, B.; Nowaczyk, G.; Jurga, S.; Jasiński, P. Graphene Oxide, Reduced Graphene Oxide and Composite Thin Films NO2 Sensing Properties. *Meas. Sci. Technol.* **2017**, *28*, 054005.

(48) Boys, S. F.; Bernardi, F. The Calculation of Small Molecular Interactions by the Differences of Separate Total Energies. Some Procedures with Reduced Errors. *Mol. Phys.* **1970**, *19*, 553−566.

(49) Pace, C. J.; Gao, J. Exploring and Exploiting Polar−π Interactions with Fluorinated Aromatic Amino Acids. *Acc. Chem. Res.* **2013**, *46*, 907−915.

(50) Salonen, L. M.; Ellermann, M.; Diederich, F. Aromatic Rings in Chemical and Biological Recognition: Energetics and Structures. *Angew. Chem. Int. Ed.* **2011**, *50*, 4808−4842.

(51) Ahmadi, A.; Hadipour, N. L.; Kamfiroozi, M.; Bagheri, Z. Theoretical Study of Aluminum Nitride Nanotubes for Chemical Sensing of Formaldehyde. *Sens. Actuators, B* **2012**, *161*, 1025−1029.

(52) Gao, K.; Zhang, X.-R.; Yu, Z.-C.; Huo, P.-Y. Structure stability and electronic properties of Pt Ir (m + n = 2-7) clusters: A DFT study. *Comput. Theor. Chem.* **2018**, *1138*, 168−175.

(53) Zhang, W.-Q.; Jin, X.-J.; Cao, H.-Y.; Tang, Q.; Wang, A.-L.; Zheng, X.-F. Molecular Structure and Absorption Spectral Properties of Corrole Isomers: DFT and TDDFT-IEFPCM Investigations. *Comput. Theor. Chem.* **2018**, *1140*, 73−79.

(54) Koul, S.; Dhawan, S. K.; Chandra, R. Compensated Sulphonated Polyaniline - Correlation of Processibility and Crystalline Structure. *Synth. Met.* **2001**, *124*, 295−299.

(55) Kondawar, S. B.; Thakare, S. R.; Khati, V.; Bompilwar, S. Nanostructure Titania Reinforced Conducting Polymer Composites. *Int. J. Mod. Phys. B* **2009**, *23*, 3297−3304.

(56) Rocha, M.; Di Santo, A.; Arias, J. M.; Gil, D. M.; Altabef, A. B. Ab-Initio and DFT Calculations on Molecular Structure, NBO, HOMO-LUMO Study and a New Vibrational Analysis of 4-(Dimethylamino) Benzaldehyde. *Spectrochim. Acta Mol. Biomol. Spectrosc.* **2015**, *136*, 635−643.

(57) Dishi, O.; Gidron, O. Macrocyclic Oligofurans: A Computational Study. *J. Org. Chem.* **2018**, *83*, 3119−3125.

(58) Laplaza, R.; Peccati, F.; A. Boto, R.; Carbone, A.; Piquemal, J. P.; Maday, Y.; Contreras-García, J.; Contreras-García, J. NCIPLOT and the Analysis of Noncovalent Interactions Using the Reduced Density Gradient. *Wiley Interdiscip. Rev.: Comput. Mol. Sci.* **2021**, *11*, No. e1497, Blackwell Publishing Inc. August 24.

(59) Lane, J. R.; Contreras-García, J.; Piquemal, J.-P.; Miller, B. J.; Kjaergaard, H. G. Are Bond Critical Points Really Critical for Hydrogen Bonding? *J. Chem. Theory Comput.* **2013**, *9*, 3263−3266.

(60) Carter-Fenk, K.; Herbert, J. M. Reinterpreting π-stacking. *Phys. Chem. Chem. Phys.* **2020**, *22*, 24870−24886.

(61) Carter-Fenk, K.; Herbert, J. M. Electrostatics does not dictate the slip-stacked arrangement of aromatic π-π interactions. *Chem. Sci.* **2020**, *11*, 6758−6765.

(62) Horn, P. R.; Mao, Y.; Head-Gordon, M. Defining the Contributions of Permanent Electrostatics, Pauli Repulsion, and Dispersion in Density Functional Theory Calculations of Intermolecular Interaction Energies. *J. Chem. Phys.* **2016**, *144*, 114107.

(63) Horn, P. R.; Head-Gordon, M. Polarization Contributions to Intermolecular Interactions Revisited with Fragment Electric-Field Response Functions. *J. Chem. Phys.* **2015**, *143*, 114111.

(64) Horn, P. R.; Head-Gordon, M. Alternative Definitions of the Frozen Energy in Energy Decomposition Analysis of Density Functional Theory Calculations. *J. Chem. Phys.* **2016**, *144*, 084118.

(65) Shao, Y.; Gan, Z.; Epifanovsky, E.; Gilbert, A. T. B.; Wormit, M.; Kussmann, J.; Lange, A. W.; Behn, A.; Deng, J.; Feng, X.; et al. Advances in Molecular Quantum Chemistry Contained in the Q-Chem 4 Program Package. *Mol. Phys.* **2014**, *113*, 184−215.

(66) Dennington, R.; Keith, T.; Millam, J. *GaussView*, version 5.0.8.; Semichem Inc.: Shawnee Mission KS, 2009.

(67) IQmol www.iqmol.org (accessed June 19, 2019).

(68) Ashraf, A.; Carter-Fenk, K.; Herbert, J. M.; Farooqi, B. A.; Farooq, U.; Ayub, K. Interaction of Graphene Quantum Dots with Oligothiophene: A Comprehensive Theoretical Study. *J. Phys. Chem. C* **2019**, *123*, 29556−29570.

(69) Gray, M.; Herbert, J. M. Simplified Tuning of Long-Range Corrected Density Functionals for Use in Symmetry-Adapted Perturbation Theory. *J. Chem. Phys.* **2021**, *155*, 034103.

(70) Mardirossian, N.; Head-Gordon, M. How Accurate Are the Minnesota Density Functionals for Noncovalent Interactions, Isomerization Energies, Thermochemistry, and Barrier Heights Involving Molecules Composed of Main-Group Elements? *J. Chem. Theory Comput.* **2016**, *12*, 4303−4325.

(71) Zhao, Y.; Truhlar, D. G. The M06 suite of density functionals for main group thermochemistry, thermochemical kinetics, noncovalent interactions, excited states, and transition elements: two new functionals and systematic testing of four M06-class functionals and 12 other functionals. *Theor. Chem. Acc.* **2008**, *120*, 215−241.

(72) Grimme, S. Density Functional Theory with London Dispersion Corrections. *Wiley Interdiscip. Rev. Comput. Mol. Sci.* **2011**, *1*, 211−228.

(73) Grimme, S.; Hansen, A.; Brandenburg, J. G.; Bannwarth, C. Dispersion-Corrected Mean-Field Electronic Structure Methods. *Chem. Rev.* **2016**, *116*, 5105−5154.

(74) Mardirossian, N.; Head-Gordon, M. Thirty Years of Density Functional Theory in Computational Chemistry: An Overview and Extensive Assessment of 200 Density Functionals. *Molecular Physics*; Taylor and Francis Ltd, 2017, Vol. 115, pp 2315−2372.

(75) Carter-Fenk, K.; Lao, K. U.; Herbert, J. M. Predicting and Understanding Non-Covalent Interactions Using Novel Forms of Symmetry-Adapted Perturbation Theory. *Acc. Chem. Res.* **2021**, *54*, 3679−3690.

(76) Mardirossian, N.; Head-Gordon, M. ωB97M-V: A combinatorially optimized, range-separated hybrid, meta-GGA density functional with VV10 nonlocal correlation. *J. Chem. Phys.* **2016**, *144*, 214110.

(77) Dasgupta, S.; Herbert, J. M. Standard grids for high-precision integration of modern density functionals: SG-2 and SG-3. *J. Comput. Chem.* **2017**, *38*, 869−882.

(78) Zade, S. S.; Bendikov, M. From Oligomers to Polymer: Convergence in the HOMO−LUMO Gaps of Conjugated Oligomers. *Org. Lett.* **2006**, *8*, 5243−5246.

(79) Ullah, H.; Shah, A.-u. -H. A.; Bilal, S.; Ayub, K. Doping and Dedoping Processes of Polypyrrole: DFT Study with Hybrid Functionals. *J. Phys. Chem. C* **2014**, *118*, 17819−17830.

(80) Ahmad, S. M.; Bibi, S.; Bilal, S.; Shah, A.-u. -H. A.; Ayub, K. Spectral and electronic properties of π-conjugated oligomers and polymers of Poly (o-chloroaniline-co-o-toluidine) calculated with density functional theory. *Synth. Met.* **2015**, *205*, 153−163.

(81) Wasim, F.; Mahmood, T.; Ayub, K. An Accurate Cost Effective DFT Approach to Study the Sensing Behaviour of Polypyrrole

towards Nitrate Ions in Gas and Aqueous Phases. *Phys. Chem. Chem. Phys.* **2016**, *18*, 19236−19247.

(82) Koopmans, T. Ordering of Wavefunctions and Eigen Energies to the Individual Electrons of an Atom. *Physica* **1933**, *1*, 104−113.

(83) Parr, R. G.; Szentpály, L. V.; Liu, S. Electrophilicity Index. *J. Am. Chem. Soc.* **1999**, *121*, 1922−1924.
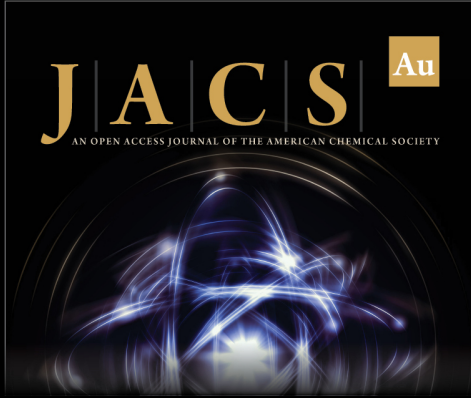
(84) O'Boyle, N. M.; Tenderholt, A. L.; Langner, K. M. cclib: A library for package-independent computational chemistry algorithms. *J. Comput. Chem.* **2008**, *29*, 839.

(85) Lu, T.; Chen, F. Multiwfn: A Multifunctional Wavefunction Analyzer. *J. Comput. Chem.* **2012**, *33*, 580−592.

(86) Humphrey, W.; Dalke, A.; Schulten, K. VMD: Visual Molecular Dynamics. *J. Mol. Graph.* **1996**, *14*, 33−38.

(87) Horn, P. R.; Mao, Y.; Head-Gordon, M. Probing Non-Covalent Interactions with a Second Generation Energy Decomposition Analysis Using Absolutely Localized Molecular Orbitals. *Phys. Chem. Chem. Phys.* **2016**, *18*, 23067−23079.

(88) Ohio Supercomputer Center. http://osc.edu/ark:/19495/f5s1ph73 (accessed June 19, 2019).